SENSORCOMM 2018

The Twelfth International Conference on Sensor Technologies and Applications

ISBN: 978-1-61208-659-0

September 16 - 20, 2018

Venice, Italy

SENSORCOMM 2018 Editors

Jaime Lloret Mauri, Polytechnic University of Valencia, Spain

SENSORCOMM 2018

Forward

The Twelfth International Conference on Sensor Technologies and Applications (SENSORCOMM 2018), held between September 16, 2018 and September 20, 2018 in Venice, Italy, continued a series of events covering related topics on theory and practice on wired and wireless sensors and sensor networks.

Sensors and sensor networks have become a highly active research area because of their potential of providing diverse services to broad range of applications, not only on science and engineering, but equally importantly on issues related to critical infrastructure protection and security, health care, the environment, energy, food safety, and the potential impact on the quality of all areas of life.

Sensor networks and sensor-based systems support many applications today on the ground. Underwater operations and applications are quite limited by comparison. Most applications refer to remotely controlled submersibles and wide-area data collection systems at a coarse granularity.

In wireless sensor and micro-sensor networks, energy consumption is a key factor for the sensor lifetime and accuracy of information. Protocols and mechanisms have been proposed for energy optimization considering various communication factors and types of applications. Conserving energy and optimizing energy consumption are challenges in wireless sensor networks, requiring energy-adaptive protocols, self-organization, and balanced forwarding mechanisms.

We take here the opportunity to warmly thank all the members of the SENSORCOMM 2018 technical program committee, as well as all the reviewers. The creation of such a high quality conference program would not have been possible without their involvement. We also kindly thank all the authors who dedicated their time and effort to contribute to SENSORCOMM 2018. We truly believe that, thanks to all these efforts, the final conference program consisted of top quality contributions.

We also gratefully thank the members of the SENSORCOMM 2018 organizing committee for their help in handling the logistics and for their work that made this professional meeting a success.

We hope that SENSORCOMM 2018 was a successful international forum for the exchange of ideas and results between academia and industry and to promote further progress in the field of sensor technologies and applications. We also hope that Venice, Italy provided a pleasant environment during the conference and everyone saved some time to enjoy the unique charm of the city.

SENSORCOMM 2018 Chairs

SENSORCOMM Steering Committee
Sergey Yurish, IFSA, Spain

Brendan O'Flynn, Tyndall National Institute | University College Cork, Ireland
Jaime Lloret Mauri, Polytechnic University of Valencia, Spain
Elad Schiller, Chalmers University of Technology, Sweden
Jiannan Zhai, Florida Atlantic University, USA
Stefano Mariani, Politecnico di Milano, Italy
Manuela Vieira, ISEL-CTS/UNINOVA, Portugal
Tadashi Okoshi, Keio University, Japan
Jerker Delsing, Lulea University of Technology, Sweden

SENSORCOMM Industry/Research Advisory Committee

Shaohan Hu, IBM Research, USA

SENSORCOMM 2018
Committee

SENSORCOMM Steering Committee

Sergey Yurish, IFSA, Spain
Brendan O'Flynn, Tyndall National Institute | University College Cork, Ireland
Jaime Lloret Mauri, Polytechnic University of Valencia, Spain
Elad Schiller, Chalmers University of Technology, Sweden
Jiannan Zhai, Florida Atlantic University, USA
Stefano Mariani, Politecnico di Milano, Italy
Manuela Vieira, ISEL-CTS/UNINOVA, Portugal
Tadashi Okoshi, Keio University, Japan
Jerker Delsing, Lulea University of Technology, Sweden

SENSORCOMM Industry/Research Advisory Committee

Shaohan Hu, IBM Research, USA

SENSORCOMM 2018 Technical Program Committee

Majid Bayani Abbasy, National University of Costa Rica, Costa Rica
Rajat Aggarwal, DreamVu Inc., USA
Amin Al-Habaibeh, Nottingham Trent University, UK
Jesús B. Alonso Hernández, Institute for Technological Development and Innovation in Communications (IDeTIC) | University of Las Palmas de Gran Canaria (ULPGC), Spain
Maykel Alonso Arce, CEIT and Tecnun (University of Navarra), Spain
Mário Alves, Politécnico do Porto (ISEP/IPP), Portugal
Andy Augousti, Kingston University, UK
Paolo Bellavista, University of Bologna, Italy
An Braeken, Vrije Universiteit Brussel, Belgium
Erik Buchmann, Hochschule für Telekommunikation Leipzig, Germany
Maria-Dolores Cano, Universidad Politécnica de Cartagena, Spain
Juan-Vicente Capella-Hernández, Universitat Politècnica de València, Spain
Vítor Carvalho, IPCA-EST-2Ai | Portugal & Algoritmi Research Centre, UM, Portugal
Luca Caviglione, National Research Council of Italy (CNR), Italy
Matteo Ceriotti, University of Duisburg-Essen, Germany
Amitava Chatterjee, Jadavpur University, India
Edmon Chehura, Cranfield University, UK
Omar Cheikhrouhou, Taif University, Saudi Arabia
Bill Chen, University of Macau, Macau
Dixiang Chen, National University of Defense Technology, China
Sungrae Cho, Chung-Ang University, South Korea
Mario Cifrek, University of Zagreb, Croatia
Victor Cionca, Cork Institute of Technology, Ireland
Gautam K. Das, Indian Institute of Technology Guwahati, India

Francesco G. Della Corte, Università degli Studi Mediterranea, Italy
Jerker Delsing, Lulea University of Technology, Sweden
Baban P. Dhonge, Indira Gandhi Center for Atomic Research, Kalpakkam, India
Alexandar Djordjevich, City University of Hong Kong, Hong Kong
Dulce Domingos, University of Lisbon, Portugal
Biyi Fang, Michigan State University, USA
Zoltan Fekete, Pazmany Peter Catholic University (PPKE), Hungary
Paulo Felisberto, LARSys | University of Algarve, Portugal
Rodrigo Ferrão de Paiva Martins, Uninova/CEMOP, Portugal
Stefan Fischer, University of Lübeck, Germany
Yann Garcia, Université catholique de Louvain, Belgium
Matthieu Gautier, IRISA | University of Rennes 1, France
Paulo Gil, University of Coimbra, Portugal
Chris Gniady, University of Arizona, USA
Arda Gumusalan, George Mason University, USA
Malka N. Halgamuge, University of Melbourne, Australia
Jason O. Hallstrom, Florida Atlantic University, USA
David Hasenfratz, Sensirion AG, Staefa, Switzerland
Mehrdad Hessar, Paul G. Allen School - University of Washington, USA
María del Carmen Horrillo Güemes, Instituto de Tecnologías Físicas y de la Información (ITEFI) | Consejo Superior de Investigaciones Científicas (CSIC), Spain
Shaohan Hu, IBM Research, USA
Chao Huang, University of Notre Dame, USA
Yanqiu Huang, University of Bremen, Germany
Raúl Igual, University of Zaragoza, Teruel, Spain
Tarikul Islam, Jamia Millia Islamia (University), India
Miao Jin, University of Louisiana at Lafayette, USA
Shuanggen Jin, Shanghai Astronomical Observatory | Chinese Academy of Sciences, China
Anand Joshi, G.H.Patel College of Engineering & Technology, India
Abdelmajid Khelil, Landshut University, Germany
Young-Jin Kim, Ajou University, Republic of Korea
Grigoris Kaltsas, Technological Educational Institute (T.E.I) of Athens, Greece
Yuriy P. Kondratenko, Petro Mohyla Black Sea State University, Ukraine
Sisil Kumarawadu, University of Moratuwa, Sri Lanka
Andrew Kusiak, University of Iowa, USA
Seongsoo Lee, Soongsil University, Korea
Shen Li, IBM Research, USA
Chiu-Kuo Liang, Chung Hua University, Hsinchu, Taiwan
Tiong Hoo Lim, Universiti Teknologi Brunei, Brunei
Thomas Lindh, School of Technology and Health - KTH, Sweden
Jingbin Liu, Finnish Geospatial Research Institute, Finland / Wuhan University, China
David Lizcano, Madrid Open University (UDIMA), Spain
Jaime Lloret Mauri, Polytechnic University of Valencia, Spain
Benny Lo, The Hamlyn Centre for Robotic Surgery | Imperial College London, UK

Beatriz López, University of Girona, Spain
Flaminia Luccio, University Ca' Foscari of Venice, Italy
Boushra Maala, Tishreen University, Syria
Elsa María Macías López, University of Las Palmas de Gran Canaria, Spain
Abdallah Makhoul, University of Bourgogne Franche-Comté, France
Piero Malcovati, University of Pavia, Italy
Ramona Marfievici, Cork Institute of Technology, Ireland
Stefano Mariani, Politecnico di Milano, Italy
José-Fernán Martínez-Ortega, Universidad Politécnica de Madrid, Spain / Mälardalen University, Sweden
Francisco Martins, University of Lisbon, Portugal
Carlo Massaroni, Università Campus Bio-Medico di Roma, Italy
Natarajan Meghanathan, Jackson State University, USA
Lei Mei,California Research Center - Agilent Technologies, USA
Carosena Meola, University of Naples Federico II, Italy
Fabien Mieyeville, University Claude Bernard Lyon 1 | Polytech Lyon, France
Umair N. Mughal, UiT The Arctic University of Norway - Campus Narvik, Norway
Dmitry Namiot, Lomonosov Moscow State University, Russia
Jagriti Narang, Amity Institute of Nanotechnology | Amity University, India
Androula G. Nassiopoulou, Institute of Nanoscience and Nanotechnology (INN), Athens, Greece
Mir Mohammad Navidi, West Virginia University, USA
Thabile Ndlovu, University of Swaziland, Kwaluseni, Swaziland
Kamen N. Nedev, University of Sofia, Bulgaria
Michael Niedermayer, Beuth University of Applied Sciences - Berlin, Germany
Shahriar Nirjon, UNC Chapel Hill, USA
Claro Noda, Mid Sweden University, Sweden
Brendan O'Flynn, Tyndall National Institute | University College Cork, Ireland
Tadashi Okoshi, Keio University, Japan
Vytautas Ostasevicius, Kaunas University of Technology, Lithuania
Carlos Enrique Palau Salvador, Universidad Politecnica de Valencia, Spain
Henryk Palus, Silesian University of Technology, Poland
Sung-Joon Park, Gangneung-Wonju National University, South Korea
Lorena Parra, Universitat Politècnica de València, Spain
Luigi Patrono, University of Salento, Italy
Nuno Pereira, School of Engineering of the Polytechnic of Porto, Portugal
Rafael Pérez del Real, Tenured Scientist at Institute of Materials Science of Madrid, Spain
Francisco Pérez-Ocón, University of Granada, Spain
Samuela Persia, Fondazione Ugo Bordoni, Italy
Ivan Pires, University of Beira Interior, Covilhã / Altran Portugal, Lisboa, Portugal
Rajeev Piyare, Bruno Kessler Foundation, Trento, Italy
Nuno Pombo, University of Beira Interior, Portugal
Patrick Pons, LAAS-CNRS, France
James Pope, University of Bristol, UK
Yuankai Qi, Harbin Institute of Technology, China

Ginu Rajan, University of Wollongong, Australia
Susan Rea, Cork Institute of Technology, Ireland
Yenumula B. Reddy, Grambling State University, USA
Càndid Reig, University of Valencia, Spain
Christos Riziotis, National Hellenic Research Foundation (NHRF), Athens, Greece
Jorge Rodolfo Beingolea Garay, Polytechnic School of the University of Sao Paulo, Brazil
Juha Röning, University of Oulu, Finland
Lorenzo Rubio-Arjona, Universitat Politècnica de València, Spain
Ulrich Rückert, Bielefeld University, Germany
Prasan Kumar Sahoo, Chang Gung University / Chang Gung Memorial Hospital, Taiwan
Addisson Salazar, Universitat Politècnica de València, Spain
Emiliano Schena, Università Campus Bio-Medico di Roma, Italy
Elad Schiller, Chalmers University of Technology, Sweden
Christian Schindelhauer, University of Freiburg, Germany
Rudi Seitz, University of New Hampshire, USA
Sheng Shen, University of Illinois at Urbana-Champaign, USA
Kuei-Ping Shih, Tamkang University, Taiwan
Amir Shirkhodaie, Tennessee State University, USA
LihChyun Shu, National Cheng Kung University, Taiwan
Patrick Siarry, Université de Paris 12, France
Marius Silaghi, Florida Institute of Technology, USA
Andrzej Skowron, University of Warsaw, Poland
Biljana Risteska Stojkoska, University Ss Cyril and Methodius Skopje, Macedonia
Mu-Chun Su, National Central University, Taiwan
Alvaro Suárez Sarmiento, University of Las Palmas de Gran Canaria, Spain
Xuyuan Tao, ENSAIT, France
Pedro Renato Tavares Pinho, ISEL - Instituto Superior de Engenharia de Lisboa | Instituto de Telecomunicações (IT-AV), Aveiro, Portugal
Rui Teng, Advanced Telecommunications Research Institute International, Japan
Sivan Toledo, Blavatnik School of Computer Science | Tel-Aviv University, Israel
Carlos Travieso González, University of Las Palmas de Gran Canaria, Spain
Janez Trontelj, University of Ljubljana, Slovenia
Ugo Vaccaro, University of Salerno, Italy
Fabrice Valois, INSA Lyon, France
Yuriy Vashpanov, Hanyang Institute of Technology - Hanyang University, Seoul, South Korea
Manuela Vieira, ISEL-CTS/UNINOVA, Portugal
Hiroo Wakaumi, Tokyo Metropolitan College of Industrial Technology, Japan
You-Chiun Wang, National Sun Yat-sen University, Taiwan
Chih-Yu Wen, National Chung Hsing University, Taiwan
Zongwei Xu, Tianjin University, China
Wanli Yu, University of Bremen, Germany
Chau Yuen, Singapore University of Technology and Design (SUTD), Singapore
Sergey Y. Yurish, International Frequency Sensor Association (IFSA), Spain
Marco Zennaro, International Centre for Theoretical Physics (ICTP), Italy

Jiannan Zhai, Florida Atlantic University, USA
Xiaohong Zhou, Tsinghua University, China
Cherif Zizoua, Research Centre for Scientific and Technical Information, Algiers, Algeria
Chengzhi Zong, Microsoft, USA

Copyright Information

For your reference, this is the text governing the copyright release for material published by IARIA.

The copyright release is a transfer of publication rights, which allows IARIA and its partners to drive the dissemination of the published material. This allows IARIA to give articles increased visibility via distribution, inclusion in libraries, and arrangements for submission to indexes.

I, the undersigned, declare that the article is original, and that I represent the authors of this article in the copyright release matters. If this work has been done as work-for-hire, I have obtained all necessary clearances to execute a copyright release. I hereby irrevocably transfer exclusive copyright for this material to IARIA. I give IARIA permission or reproduce the work in any media format such as, but not limited to, print, digital, or electronic. I give IARIA permission to distribute the materials without restriction to any institutions or individuals. I give IARIA permission to submit the work for inclusion in article repositories as IARIA sees fit.

I, the undersigned, declare that to the best of my knowledge, the article is does not contain libelous or otherwise unlawful contents or invading the right of privacy or infringing on a proprietary right.

Following the copyright release, any circulated version of the article must bear the copyright notice and any header and footer information that IARIA applies to the published article.

IARIA grants royalty-free permission to the authors to disseminate the work, under the above provisions, for any academic, commercial, or industrial use. IARIA grants royalty-free permission to any individuals or institutions to make the article available electronically, online, or in print.

IARIA acknowledges that rights to any algorithm, process, procedure, apparatus, or articles of manufacture remain with the authors and their employers.

I, the undersigned, understand that IARIA will not be liable, in contract, tort (including, without limitation, negligence), pre-contract or other representations (other than fraudulent misrepresentations) or otherwise in connection with the publication of my work.

Exception to the above is made for work-for-hire performed while employed by the government. In that case, copyright to the material remains with the said government. The rightful owners (authors and government entity) grant unlimited and unrestricted permission to IARIA, IARIA's contractors, and IARIA's partners to further distribute the work.

Table of Contents

Integrated Security for Embedded IoT Systems

Paul Fortier, Patrick DaSilva, Benjamin Viall
Electrical and Computer Engineering Department
University of Massachusetts Dartmouth
North Dartmouth, Massachusetts USA
email: pfortier@umassd.edu, pdasilva@umassd.edu, u_bviall@umassd.edu

Abstract— **Embedded systems within the evolving Internet of Things (IoT) space are becoming ubiquitous. The problem lies in their weak to non-existing security. Embedded IoT systems can be built as Systems on a Chip (SoC) using IP-cores and Field Programmable Gate Array (FPGA) technology, as components within a Printed Circuit Board (PCB) or as systems of systems. In each case there are different levels of design as well as security vulnerabilities and therefore solutions. This paper looks into hardware, firmware and software security issues as well as techniques to improve an embedded systems overall security for a subsurface roadway IoT sensing system.**

Keywords-Embedded systems; security; IP-Cores; SoC.

I. INTRODUCTION

Embedded computer systems are found in just about every object engaged in smart and connected cities activities. Embedded systems typically operate within real-time processing constraints and must process input data in a timely manner to drive output data or control physical actions. Embedded systems are designed to operate typically without human interaction. In some instances embedded systems may respond to human inputs to steer the actions of one or more deeply embedded systems. When designing embedded systems, the typical mode of operation, is to determine what physical parameters are needed to meet systems goals and design elements to support these requirements.

This paper provides a descriptive overview of an architecture and design for a wireless underground smart sensor system, data collection and Internet of Things (IoT) transmission system. The subsurface sensing system under test at the University of Massachusetts is presently being modified to investigate and include security management through all levels of the architecture where deemed necessary. The paper will examine issues encountered during the development of hardware security elements.

Section II defines the application used to motivate security needs for embedded systems. Section III introduces security concepts and how they apply to embedded systems. Section IV describes the proposed conceptual solution both hardware and software. Followed by Section V where the papers conclusions are drawn.

II. ROADWAY SENSING SYSTEM APPLICATION

Several million miles of secondary paved and unpaved roads in the United States lie in seasonal frost areas and are highly susceptible to damage during the winter freeze and spring thaw periods. To understand roadway structural conditions during these cyclic periods requires knowledge concerning subsurface temperature and moisture. Though, acquiring roadway subsurface information in real-time is costly, difficult and in some cases, impossible given currently available technologies.

Roadway management policies such as seasonal load restriction (SLR), limits loads of heavy trucks during the spring thaw period. Roadway restrictions may cause trucks to take costly detours requiring additional driving time and lighter loads resulting in more trips. The challenge is to protect the transportation infrastructure and minimize roadway maintenance costs, but also to allow commerce to flow as unrestricted as possible during spring thaw and roadway strength recovery periods.

Present methods for imposing SLR's are not real-time nor data driven. Most rely on using cumulative thawing index [1] based on computed degree day measurement. Additional studies [2]-[4] looked to reduce the time SLR is in place using manual collection methods and models. State Department of Transportation (DOT's) have performed studies looking at methods to remove SLR's in a timely fashion [5]-[7] using measured data.

One system design consideration not addressed in the initial study was the issue of sensor site and communications node security. To address those deficiencies, a redesign of the sensor node and communications node to include hardware based mechanisms for detection, response and recovery from malicious attacks has been initiated.

A. Roadway Sensing System Architecture

Researchers [9]-[11] examined using wireless sensors to monitor subsurface environmental conditions. The University of Massachusetts Dartmouth (UMD) SLR forecasting tool builds upon this research using real-time data feeds from wireless sensors embedded in managed roadways using semi-automated techniques [12]-[14]. The hardware for the UMD SLR system consists of embedded subsurface roadway sensors and IoT communications nodes linked with a backend Decision Support System (DSS) (Fig. 1).

ISBN: 978-1-61208-659-0

Wireless sensors are embedded into roadways to a depth of up to nine feet. Sensors are recharged using a multi-source recharging subsystem. Collected data is packaged and transmitted to the UMD decision support system (Fig. 2).

The UMD SLR DSS system consists of data extraction, fusion, visualization and infrastructure forecasting tools. Data extraction tools retrieve data feeds, translate and package raw data for decision support tool use. Extracted data include site specific weather data, embedded sensor data and site soil composition data.

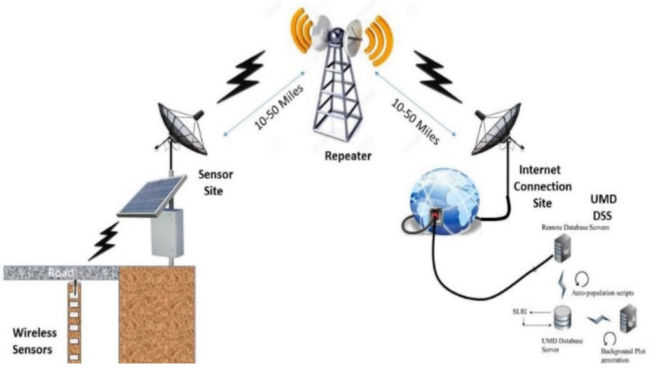

Figure 1. UMD SLR Systems Architecture

B. *Subsurface Roadway Sensor Design*

The wireless sensor nodes (Fig. 2) are constructed using three custom Printed Circuit Boards (PCB) with custom Field Programmable Gate Arrays (FPGA) supporting required data collection, processing and transmission. One PCB is used to read and manage sensor data access, a second to manage power generation and a third to manage system interactions.

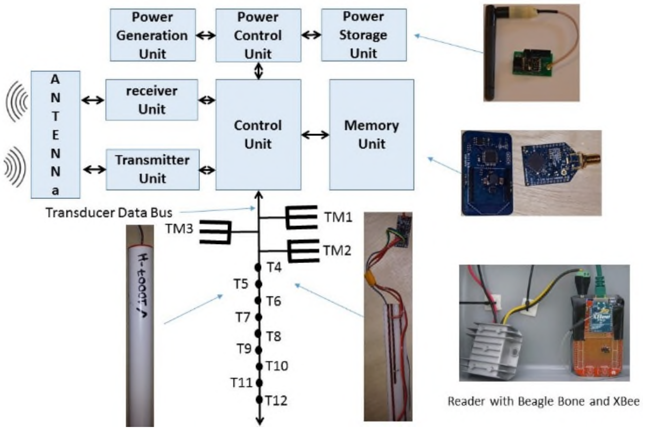

Figure 2. Wireless Smart Sensor Architecture

The sensor communications node operates at 900 MHz with a data rate of 200 kbps. The communications component is connected to an embedded FPGA based controller responsible for interacting with the sensors to extract measurements, convert information and package for transmission to the external reader on demand. The last component is the power management board using power harvesting elements to maintain battery power. Supporting the sensor system is a roadside solar battery powered reader. The reader uses a commercial radio frequency communications module and a Linux processor to implement IoT connectivity to the DSS (Fig. 2).

III. EMBEDDED SYSTEMS SECURITY ISSUES

Security has been talked about for quite some time as more IoT devices spread throughout the ecosystem of the smart and connected cities concept. Even prior to the notion of inter-connection of IoT devices for anywhere / any time access, security was a concern from system developers, though not often for the single IoT sensor developed by small vendors. As IoT devices become ubiquitous, security flaws have begun to be exposed and now thought of as being important to consider. To examine what a security flaw looks like as well as the reasons for an attack an existing security taxonomy [15] was refined to focus embedded systems vulnerabilities.

The taxonomy defines what a security incident is, what the attack was and how the attack was carried out. The taxonomy defines, the attacker, tools used, form of access to the target, what vulnerability was used, what action was taken by the attacker, what the target of the attack was, the objectives and result of the attack, and the actual harm inflicted. The taxonomy has helped in focusing understanding of vulnerabilities and to work towards developing solutions.

A. *Security Flaws in Embedded Systems*

Embedded systems typically interact with some physical system to provide a strict timing response to stimuli. Failure to adhere to timing constraints effects real-time response, performance, and ultimately the safety and security of the embedded application. Typical characteristics of embedded systems such as; limited core processing power, limited available power, physical exposure, remoteness, unmanned operation, and network connectivity represent possible limitations as well as cybersecurity weaknesses. Embedded systems limited resources imply they lack excess capacity to support security services operations adequately [16].

Limited resources within embedded systems also provide the attacker with areas to exploit. For example, many embedded systems utilize FPGA open cores supporting local processing, input, output and storage, which may harbor malicious elements or unobstructed open entry points (Fig. 4). Embedded systems limited resources make them vulnerable to denial of service attacks, power depletion attacks, code reuse attacks and memory hacking attacks to name a few. Limited operating system services, tightly timed applications task segments as well as limited controls on memory access, inputs and outputs may also provide the attacker numerous targets for their interference (Fig. 3). One such attack, referred to as a code reuse attack, causes control flow changes by reusing existing instructions for malicious purposes. Typically code reuse attacks modify non-executable memory by overwriting stacks, function pointers, or set jump buffers forcing the processor to execute instructions in unintended sequences or into regions not tested during normal system verification and validation. Numerous authors have written about the need for hardware based solutions to embedded System on a Chip (SoC) security vulnerabilities [17].

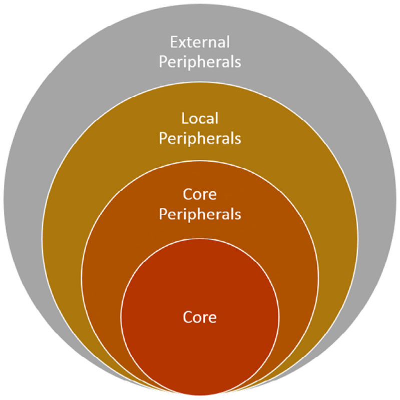

Figure 3. Onion model for system on a chip IoT devices

De Clercq and Verbauwhede published a survey of 21 hardware-based Control Flow Integrity (CFI) architectures [17] that describes the need for hardware-based over software-based CFI solutions. Software-based CFI solutions rely on inserting code into a program to perform CFI checks on indirect branches. When the compiler is unaware of the security aspects concerning the CFI checks, it might cause the optimization step to spill registers holding sensitive CFI data to the stack [17]. The attacker model expects the attacker to always have control of data memory and hence the stack allowing the attacker to circumvent the CFI protections. Hardware-based access control mechanisms can provide strong isolation for runtime data structures and metadata [17]. Hardware-based architectures can protect against attackers that control both code and data memory.

The analysis of the security policies used included a detailed comparison of the policies with respect to their security, limitations, hardware cost, performance, and practicality. In general, the use of a Shadow Call Stack (SCS) is particularly important to protecting the backward edge of control flow against Return-Oriented Programming (ROP). De Clercq and Verbauwhede concluded the forward edge of the control flow still face practical limitations preventing widespread adoption. More than half require software components placed inside the binary causing reduced responsiveness to real time tasking, opening them up to code injection attacks if non-executable memory protections are not enforced. Of the 21 CFI architectures, 75% of them focused on x86, ARM, or SPARC Instruction Set Architecture (ISR) as the target and one focused on the AVR ISR [18]. Of the 17 CFI architectures that contained a forward edge static policy, branch regulation and table policies met the most protection requirements. However, both branch regulation and table policies either require complex control flow graphs or software placed inside the binary.

B. *Security Solutions for Embedded systems*

A Framework for Improving Critical Infrastructure Cybersecurity [15] version 1.1 released in April 2018 is the outcome of the National Institute of Standards and Technology (NIST) collaborating with private and government entities to provide cybersecurity risk frameworks for voluntary use by critical infrastructure owners and operators. The Framework offers a way to address cybersecurity's effect on physical, cyber, and people. The framework is applicable to organizations relying on technology such as industrial control systems (ICS), Cyber-Physical Systems (CPS), and the Internet of Things (IoT). The core of the Framework consists of five functions or basic cybersecurity activities – Identify, Protect, Detect, Respond, and Recover.

- Identify – Develop an organizational understanding to manage cybersecurity risk to systems, people, assets, data, and capabilities.
- Protect – Develop and implement appropriate safeguards to ensure delivery of critical services.
- Detect – Develop and implement appropriate activities to identify the occurrence of a cybersecurity event.
- Respond – Develop and implement appropriate activities to take action regarding a detected cybersecurity incident.
- Recover – Develop and implement appropriate activities to maintain plans for resilience and to restore any capabilities or services that were impaired due to a cybersecurity incident.

Under the Framework, the proposed subsurface roadway sensor system's solution attempts to provide Protect, Detect, Respond, and Recover mechanisms to support an embedded system under cyber-attack while maintaining system integrity and mission essential functionality. The proposed solution seeks to protect an embedded processor by detecting unexpected control flow changes using hardware-based control flow integrity techniques integrated into the Security Unit (SU). The Security Memory (SM) contains a merged file containing meta-data from an off-line control flow analysis merged with the FPGA bit stream to aid in recovery. The response to a malicious detection is to isolate the malicious control flow changes by redirecting them to a SACrificial processor (SAC) to prevent and avoid further infection of the embedded system (Fig. 5). The SAC also has a SAC Data Memory (SACDM) to isolate Data Memory (DM) from malicious alterations. Actions of the SAC are recorded in the data output unit (DOU) for post run analysis.

The conceptual design strives to detect attacks, respond to attacks in a way that prevents future or continuous successful attacks identified through real-time instruction analysis and data storage analysis techniques under development within this project.

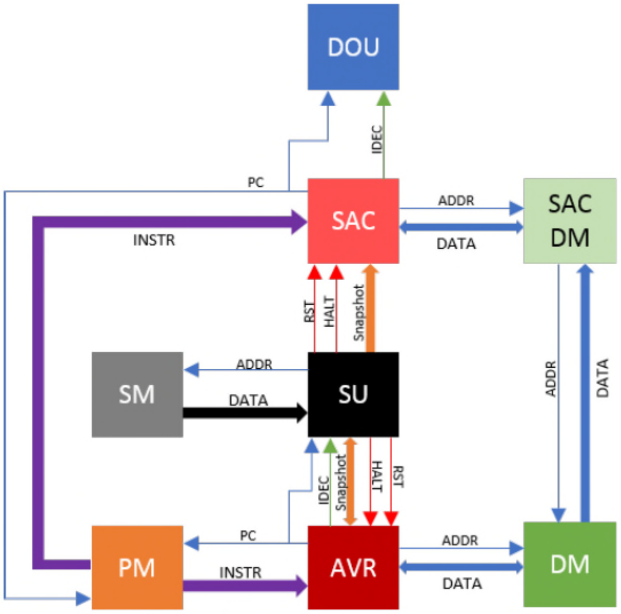

Figure 4. Conceptual Embedded SoC secure architecture

IV. SLR ROADWAY IOT SECURITY SOLUTION METHODS

As depicted in Fig. 4 above, our hardware (FPGA) based solution uses a variety of added hardware elements to monitor activity, detect erroneous activity, respond to the malicious activity and recover embedded systems normal operations. A hardware element, the Security Unit (SU) monitors instruction formats, jump and branching addresses using a novel associative search engine to identify rogue instructions not found in valid code blocks as well as invalid jump and branch addresses injected by malicious means.

One such attack is a Control Flow Attack (CFA). CFA's include Code Reuse Attacks (CRAs) and Code Injection Attacks (CIA). An example of an altered control flow can be seen in Fig. 5. Using a control flow graph, the steps through a process can be visualized as a set of directed edges and nodes. An unaltered running process will follow the correct forward and backward edges of its control flow. Any redirection of an edge would cause a control flow violation.

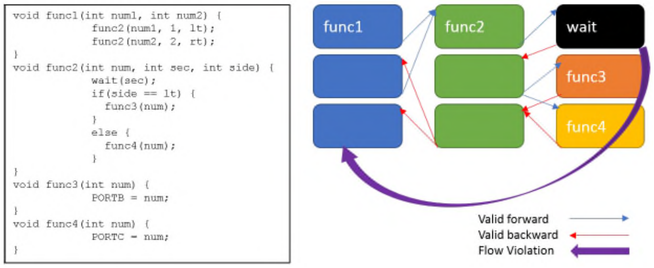

```
void func1(int num1, int num2) {
            func2(num1, 1, lt);
            func2(num2, 2, rt);
}
void func2(int num, int sec, int side) {
            wait(sec);
            if(side == lt) {
              func3(num);
            }
            else {
              func4(num);
            }
}
void func3(int num) {
            PORTB = num;
}
void func4(int num) {
            PORTC = num;
}
```

Figure 5. Example control flow graph.

To aid in detection of control flow violations, meta-data from an off-line control flow analysis conducted on the program binary is loaded into the security memory (SM) through a merging process with the FPGA bit stream file. This avoids the need to re-synthesize the FPGA bit stream due to a security recovery scenario. When the FPGA powers on, pre-build control flow meta-data is loaded from the SM into the SU.

Detection is done using a hardware-based CFI solution assuming CRAs. At a minimum the CFI solution will monitor AVR direct, indirect, and relative branch instructions (jmp, call, ret) to determine any violations in the intended control flow at the function block level.

Each time a valid function block is called, a snapshot of the core is taken. Since the PM can't be modified by an attacker, the detected malicious instruction happened in the called function block through a data memory exploit. Upon detection, a previous valid snapshot is loaded into the AVR core. The embedded core continues processing from a state before the attack happened. If the same malicious instruction is encountered, then a reset occurs, clearing out any bad data in the DM.

If a code injection attack is detected, partial or whole portions of the program memory will be reloaded to recover the system to a usable state. To support reloading program memory, the recovery scheme requires an additional copy of the original program binary. The best case scenario would be code injected outside the program binary bounds. In this scenario, only a checkpoint recovery may be needed. The worst case scenario is injected code within the program binary area. This would result in pausing execution to reload program memory and restarting the soft-core from a checkpoint or reset state.

Once malicious code is identified, the system moves active malicious code execution to a sacrificial processor that continues to run the malicious code and collect data, to the Data Output Unit (DOU), to aid in analysis of the malicious code off line. Recovery will be accomplished using clean binaries, stored in the security memory (SM), which are reloaded into the devices primary program memory.

Presently a prototype system on a chip (Fig. 4) implementing an 8-bit Alf and Vegard's RISC (AVR) soft-core processor on a Xilinx Artix 7 series FPGA has been constructed. Further refinement and testing should be completed by the time of the conference.

V. CONCLUSION

In this paper, we described the problem facing federal, state, municipalities and companies in management of roadway assets during times of fluctuating weather conditions to limit damage due to heavy trafficking on their managed roads using load restrictions. The paper describes a system developed to meet the need of placement and removal of SLR's. Described within is the high level systems architecture, sensor, reader and communications architectures used to validate systems operations. The system as presently deployed lacks adequate security from cybercriminal activity. To remedy this situation a study is ongoing to redesign the FPGA based components and PCB's in order to integrate security at the core hardware level. The goal being to provide policies and mechanisms to support identification of potential security flaws in the design, develop hardware based detection of malicious activities, to develop hardware solutions supporting response to such attacks and mechanisms to recover to an operational mode after an attach event in near real-time.

ACKNOWLEDGMENT

The project basic sensor development was partially funded by the USDOT Office of the Assistant Secretary for Research and Technology, U.S. Department of Transportation, under grant OASRTRS-14-H-UMDA. The views, opinions, findings and results presented are those of the authors and do not reflect official policy or position of our sponsor, the USDOT/OST-R, or any State or other entity.

REFERENCES

[1] A. H. Bradley, M. A. Ahammed, S. Hilderman and S. Kass, Responding to Climate Change with Rational Approaches for Managing Seasonal Weight Programs in Manitoba. Proceedings of the American Society of Civil Engineers 15th International Conference on Cold Regions Engineering. CD-ROM. Quebec City, Canada, August 19-22, pp. 391 – 401, 2012.

[2] Minnesota Department of Transportation (Mn DOT), "Policy and Process for Seasonal Load Limit Starting and Ending Dates," Minnesota Department of Transportation, Policy, Safety & Strategic Initiatives Division, Technical Memorandum No. 09-09-MAT-02, June 29, 2009.

[3] R. Embacher, "Duration of Spring Thaw Recovery for Aggregate-Surfaced Roads," Transportation Research Record: Journal of the Transportation Research Board No 1967, pp. 27-35, Transportation Research Board of the National Academies, Washington D.C., 2006.

[4] G. L. Hanek, M. A. Truebe and M. A. Kestler, Using Time Domain Reflectometry (TDR) and Radio Frequency (RF) Devices to Monitor Seasonal Moisture Variation in Forest Road Subgrade and Base Materials, U.S. Department of Agriculture, Forest Service, San Dimas Technology and Development Center, San Dimas, CA, 2001.

[5] R. A. Eaton et al., "Spring Thaw Predictor and Development of Real Time Spring Load Restrictions," Proceedings of the American Society of Civil Engineers 14th International Conference on Cold Regions Engineering, Duluth, MN, August 30-September 2, 2009.

[6] R. A. Eaton, R. L. Berg, A. Hall, H. J. Miller and M. A. Kestler, "Initial Analysis of the New Hampshire Spring Load Restriction Procedure," Proceedings of the American Society of Civil Engineers 14th International Conference on Cold Regions Engineering, Duluth, MN, August 30-September 2, 2009.

[7] M. A. Kestler, et al., "Determining When to Place and Remove Spring Load Restrictions on Low Volume Roads: Three Low-Cost Techniques." Low Volume Roads Conference, Austin, TX, Transportation Research Record 1989, pp 219-229, WA, DC. June 2007.

[8] K. Ashton, "That 'Internet of Things' Thing." In: RFID Journal, 22 July 2009. Retrieved 17 December 2012.

[9] K. Dziadak, J. Sommerville and B. Kumar, "RFID based 3D buried assets location system." Journal of Information Technology in Construction, Vol. 13, pp. 155–165, 2008.

[10] F. Faridazar and N. Lajnef, "Intelligent multi-sensor measurements to enhance pavement monitoring and safety." In Passive Wireless Sensor Tag Workshop. NASA, Houston, 2011.

[11] M. Roberti, "RF sensors could optimize crop irrigation." RFID J. Mag. Online. http://www.rfidjournal.com/magazine/article/8172, accessed 12.17.2012.

[12] B. Marquis, "Mechanistic Approach to Determine Spring Load Restrictions in Maine," Technical Report No. 08-1, Maine Department of Transportation, Bangor, Maine, 2008.

[13] J. M. Ovik, J. A. Siekmeier, and D. A. Van Deusen, 'Improved Spring Load Restriction Guidelines Using Mechanistic Analysis," Technical Report, Minnesota Department of Transportation, 2000.

[14] R. A. Eaton, M. A. Kestler, and A. Hall, "Spring Thaw Predictor & Development of Real Time Spring Load Restrictions, First Two-Year Data Report," SP&R Research Project No. 14282K, New Hampshire Department of Transportation, Concord, NH, 2009.

[15] CI Cybersecurity, "Framework for Improving Critical Infrastructure Cybersecurity, Version 1.1," National Institute of Standards and Technology, 2018.

[16] S. Parameswaran and T. Wolf, "Embedded systems security - an overview," Design Automation for Embedded Systems, vol. 12, pp. 173-183, 2008.

[17] R. de Clercq and I. Verbauwhede, "A survey of Hardware-based Control Flow Integrity (CFI)," ACM Computing Surveys, pp: 27, 2017.

[18] A. Francillon, D. Perito and C. Castelluccia, "Defending embedded systems against control flow attacks," in Proceedings of the first ACM workshop on Secure execution of untrusted code, pp: 19-26, 2009.

Event Detection Using Abductive Reasoning on Sensor Data

Bill Karakostas
VLTN BBVA
Antwerp, Belgium
bill.karakostas@vltn.be

Abstract— **We present an approach that detects physical events such as a fire or an explosion using sensor data fusion, where not all relevant signals describing the event are available due to non-presence or malfunctioning of some sensors. We employ abductive probabilistic reasoning to detect the occurrence of an event amongst several alternative events from imperfect sensor data. Influenced by Dempster-Shafer's evidence theory, we reason on the available evidence produced by the sensor data, combined with counterevidence, to establish degrees of confidence to the different hypotheses made about the occurrence of an event. The paper also describes an experimental sensor setup for detection of fire and explosion events, and its effectiveness in terms of false negative and false positive detection rates.**

Keywords- sensor data fusion; event detection; abductive reasoning; Raspberry Pi.

I. INTRODUCTION

Sensor data fusion is the method of combining data from homogeneous or heterogeneous multiple sensors in order to form a unified picture [1]. Compared to data obtained from single sensors, multisensor data fusion improves the overall event detection capabilities, in terms of reduction in the false positive and false negative detection rates. Data fusion systems are now widely used in various areas such as sensor networks, robotics, video and image processing, and increasingly so, in Internet of Things (IoT) applications such as smart cities [2].

However, in sensor deployments, some detection capabilities may not be available because of lack of suitable sensors or because of the quality (precision, accuracy, reliability) of the obtained sensor data. Hence, false positives which means detection of a non-existing event, or false negatives which means failure to detect an event, may occur.

Therefore, intelligent processing of sensor data may be needed to rectify such deficiencies. Inference on the sensor data entails the ability to (a) detect that an event has occurred and (b) determine the type of this event amongst a number of possible event types. Logic based approaches have been employed for such purposes, however not all types of logical inferences are possible, due to incomplete data and/or weak causal relationships between an event and its manifestations. Because deductive inferencing of the event from its manifestations is not always justifiable, forms of inductive (probabilistic) [3] and abductive reasoning [4] have been employed. In this paper, we employ a variant of the later form of reasoning, which calculates evidence about the occurrence of an event from sensor data obtained from multiple sensors, and also counter-evidence from lack of observed data. Each type of sensor data is assigned a numerical weight to indicate the degree to which presence of such data supports the evidence about the occurrence of an event. Evidences and counter-evidences are compared using likelihood ratio methods, across the range of possible events, in order to find the event with the highest evidence ratio. Additionally, confidence in the suggested event detection is calculated in terms of sensitivity and specificity of the sensor layout used for event detection.

The structure of the paper is as follows. The next section presents related work, while the theoretical model for our sensor event detection method is introduced in Section III. Section IV discusses an experimental setup and experiment results for detecting and classifying smoke and explosion events from sensor data. This section also analyses the effectiveness of the approach. Section V discusses the advantages and limitations of the proposed approach to event detection and classification from sensor data, and proposes future research.

II. RELATED WORK

The approach described in this paper aims to provide a reliable way for detecting and classifying physical phenomena (events) from fused data collected from potentially unreliable measurements/sensors, to which different weights are assigned as evidence. By applying evidence-based theory, we attempt to calculate and compare the likelihoods of occurrence for the different types of events. To compensate for measurement/sensor unreliability we combine the evidence from multiple events, including the absence of evidence. Other approaches have also utilised Dempster Schafer theory for sensor data fusion [6]. Also, some approaches combine the Dempster- Shafer evidence theory with other machine learning techniques such as hierarchical neural networks, to improve the accuracy of classifications [7].

III. THEORETICAL MODEL

Physical events as opposed for example to events occurring in the digital domain, are characterised by physical processes and their quantities (energy, light, sound). For example, a fire is manifested usually by an increase in the ambient temperature and the presence of gasses. However, the manifestations of different instances of an event may vary. For example, although fires in general produce smoke, depending on the type of materials combusted, some fires may produce very little or no smoke. The intensity of the heat, the volume and composition of smoke and other physical characteristics are also subject to many parameters in the environment of the fire. Also, different types of events may have similar manifestations, for example both a fire and an explosion may produce smoke. Finally, there are detection (e.g. accuracy) limitations imposed by the technology used to manufacture the sensors, the sensor deployment layout, as well as by possible sensor malfunctioning. Such limitations can restrict our ability to use sensor data, by failing to detect an event (false negative), falsely detect an event that did not occur (false positive), or by wrongly classifying an event. Therefore, our model addresses the inherent uncertainty in event detection from sensor data and employs a probabilistic approach, influenced from concepts from Dempster-Shafer evidence theory [4] to reason on the available evidence produced by the sensors and combine it with counterevidence to establish degrees of confidence in the various hypotheses made about the occurrence of events.

It must be noted that evidence theory has been utilised for similar purposes such as diagnostic tasks where information is also obtained from sensors [5]. However, our aim is to obtain reliable information by fusing a mixture of both reliable and unreliable data and also from lack of data measurements.

Our approach is formally described as follows: Let E be the set of all types of phenomena we consider for detection and classification and M the set of all manifestations of events in E, detectable by our sensors, with each e in E characterised by a set of manifestations $\mathrm{M}_e \subset M$. We define a weighting function w_e that for every m in M_e assigns a value in {0,1} to m. The weight produced by function $\mathrm{w}_e(m)$ represents the degree to which observation of manifestation m increases the evidence that phenomenon e is occurring. We also define weights to measure *lack of evidence* i.e. the degree to which non-observation of a manifestation supports the evidence that the phenomenon has not occurred. Thus, w assigns a weight in {0,1} for each non-manifestation $\neg m$ as a measure of the evidence that the lack of a manifestation provides to support that the phenomenon has not occurred.

Note that the values for evidence and counterevidence do not have to be correlated. For example, the sensing of heat is a strong indicator that a fire has occurred, however the absence of heat detection is not an equally strong indicator that a fire has not occurred, as some fires initially do not produce measurable heat, or there is a possible malfunction of the heat sensing sensor.

Finally, we define the total evidence from our observations $O_e \subset \mathrm{M}_e$ and also from the lack of them i.e. $\grave{O}_e = \mathrm{M}_e - O_e$ about a phenomenon of type e with manifestations M_e as

$$Ev(e) = \sum\nolimits_{m \in O_e} w(m) \qquad (1)$$

$$Ev(\neg e) = \sum\nolimits_{m \in \grave{O}_e} w(m) \qquad (2)$$

The two formulas for evidence and counterevidence allow us to reason in a qualitative manner about the likelihood of a phenomenon as well as to compare the likelihoods of different phenomena. For example, even if the counterevidence for a phenomenon is zero, it is not justifiable to conclude that the phenomenon has occurred, if the gathered evidence for the phenomenon is also small. The ratio of evidence to counterevidence is an indicator of the degree of certainty from the observations. In particular, if $\mathrm{Ev(e)} \sim \mathrm{Ev}(\neg \mathrm{e})$ it indicates uncertainty as to whether the phenomenon has occurred or not. If the evidence weight Ev(e) is equal to the theoretical maximum $|\mathrm{M}_e|$ i.e. $O_e = \mathrm{M}$, then there is perfect evidence, as by necessity $\mathrm{Ev}(\neg \mathrm{e})$ has to be zero. Correspondingly, total lack of evidence occurs when $\mathrm{Ev}(\neg \mathrm{e}) = |\mathrm{M}_e|$.

To further strengthen the confidence in the diagnosis of events, prior knowledge about the frequency of occurrence of different events, if available, can be utilised. This can be expressed as a probability value *P(e)* with values in {0,1}. Probabilities are used as prevalence values for calculating likelihood ratios as explained in the next section.

As different types of events may have similar manifestations, we are often interested in being able to determine which is the most likely event has occurred, i.e. to correctly classify events. We are also interested in not falsely identifying an event (false positive) and avoid failing to detect an event (false negative) For this purpose, we utilise likelihood ratios.

We define likelihood ratio (LR) as the ratio of the probability that the event has been correctly identified, to the probability that the event has been incorrectly identified. We use sensitivity and specificity of the measurements as the numbers used to generate a LR. Sensitivity is the proportion of truly occurred events that are identified as such by the system (i.e. their total evidence scores are the highest amongst all candidate events). Specificity is the proportion of non-events that have been correctly identified and indicate the probability that the test will correctly identify a non-event.

We calculate LR for both positive and negative event identifications, expressed as 'LR+' and 'LR-', respectively. The calculations are based on the following formulas:

$$\text{LR+} = \text{sensitivity} / 1\text{- specificity} \quad (3)$$

$$\text{LR-} = 1\text{- sensitivity} / \text{specificity} \quad (4)$$

IV. EXPERIMENTATIONS

A. Experimental apparatus

We have empirically validated our approach in a sensor setup to detect and classify fire and explosion events. Fig. 1 shows the experimental device setup. On the left of the picture there is a Raspberry Pi Model B single board computer, with a GrovePi sensor HAT ('hardware at top') board, to which GrovePI sensors for atmospheric pressure, air quality, light intensity, sound and temperature are attached (some of the sensors are visible at the left of the picture). Small scale fires and explosions were produced under controlled conditions, in order to obtain the experimental data. Data were collected from the sensors periodically and stored by the Raspberry Pi where they are analysed for event detection. An event is detected, if the rate of increase in the values read by the sensor exceed a threshold, the rate of change is calculated using the five point formula $r_t = (v_{t-2} - 8v_{t-1} + 8v_{t+1} - v_{t+2})/12$, where v_t are data measurements at different timepoints. Fig. 2 shows examples of time series of collected sensor data that shows the manifestations of the different events (air pressure, temperature and light intensity), through the increase in rates in the recorded sensor values. The two events share some manifestations, for example heat, but no change to the air pressure. Additionally, the weights assigned to each manifestation differ per event. We assume that weights are assigned to manifestations by experts and that the specifics of the environment where the sensors are deployed are taken into account, to calibrate the values of the weights.

Figure 1. Apparatus used for experiments.

B. Assigning weights to phenomena

Table I demonstrates the above approach in the modelling of two physical events, a fire and an explosion. The two events share some manifestations such as heat but not others, for example, air pressure. Additionally, the weights assigned to each manifestation differ per event. We assume that weights are assigned to manifestations by experts and that the specifics of the environment where the sensors are deployed are taken into account.

C. Calculating Evidences

Table II shows the aggregated evidences for the two types of events, as well as for their negations (non-events). Additionally, the second column of Table II shows the manifestations detected by the sensors, and the third column of Table II shows the mechanisms used to generate fire and explosion manifestations.

The experiment results were used to evaluate the detection and classification capabilities of our system. In experiment #2, although the evidence of fire is overwhelming compared to counterevidence, the system cannot clearly make the case for or against an explosion with weights of 1.4 and 1.3, respectively. In experiment #3, the system narrowly suggests the hypothesis of fire over non-fire, while clearly rejects the hypothesis of an explosion. Evidence for and against fire are however (correctly) insufficiently high for the fire hypothesis to be strongly suggested.

D. Likelihood ratios, sensitivity and specificity calculations

The purpose of the experiments was to estimate the detection accuracy of our approach. Detection accuracy is the percentage of correct event detections when taking into account the total percentage of false positives and false negatives. A detection accuracy of 100% would imply a 0% false positives and false negatives rate, but may not necessarily imply zero classification errors, as explained below.

Classification errors refer to the number of misdiagnoses made during the experiment. To calculate the relevant likelihood ratios, prevalence of the explosion and fire events were set to 0.01 and 0.05 respectively, meaning that in general, 1% of detected events are true explosions and true fires respectively, also suggesting that fires are five times more common than explosions. From the data of Table II, specificities and sensitivities for fire and explosion were calculated, and then Formulas (3) and (4) were applied to calculate positive and negative likelihoods (LR+, LR-). The results are summarised in Table III.

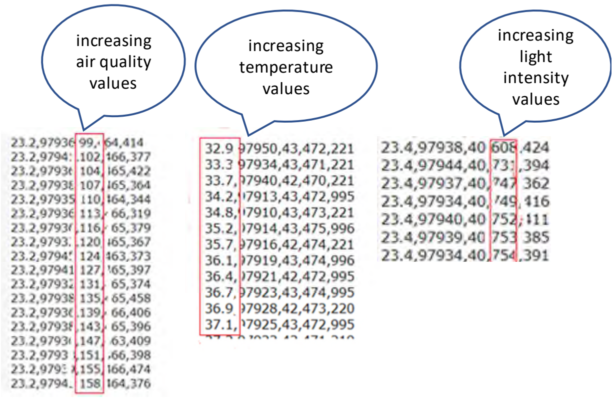

```
23.2,97936 99, 64,414
23.2,9794: 102, 166,377
23.2,9793( 104, 165,422
23.2,9793E 107, 165,364
23.2,97935 110, 164,344
23.2,97936 113, 66,319
23.2,9793( 116, 65,379
23.2,9793: 120 165,367
23.2,9794! 124 163,373
23.2,97941 127, 165,397
23.2,97932 131, 65,374
23.2,97938 135, 65,458
23.2,9793( 139, 66,406
23.2,9793E 143, 65,396
23.2,9793( 147, 63,409
23.2,9793 151, 66,398
23.2,9793 155, 166,474
23.2,9794. 158 164,376
```

```
32.9 97950,43,472,221
33.3 97934,43,471,221
33.7, 97940,42,470,221
34.2, 97913,43,472,995
34.8, 97910,43,473,221
35.2, 97914,43,475,996
35.7, 97916,42,474,221
36.1, 97919,43,474,996
36.4, 97921,42,472,995
36.7, 97923,43,474,995
36.9 97928,42,473,220
37.1, 97925,43,472,995
```

```
23.4,97938,40 608 ,424
23.4,97944,40,731 ,394
23.4,97937,40,747 362
23.4,97934,40,749,416
23.4,97940,40 752,411
23.4,97939,40 753 385
23.4,97934,40,754,391
```

Figure 2. Time series of sensor data showing manifestation of phenomena. Highlighted areas from left to right show how values for: air quality (smoke), temperature and light intensity are increasing due to the event occurrence.

TABLE I. SENSITIVITIES, SPECIFICITIES AND LIKELIHOOD RATIOS (+/-) FOR FIRE AND EXPLOSION EVENTS

Event Type	*Sensitivity*	*Specificity*	*LR+*	*LR-*
Fire	1/4	0	1/4	n/a
Explosion	3/4	1/2	3/8	1/8

TABLE II. SENSITIVITIES, SPECIFICITIES AND LIKELIHOOD RATIOS (+/-) FOR FIRE AND EXPLOSION EVENTS

Event Type	*Sensitivity*	*Specificity*	*LR+*	*LR-*
Fire	1/4	0	1/4	n/a
Explosion	3/4	1/2	3/8	1/8

TABLE III. EVIDENCE AND COUNTEREVIDENCE FOR DIFFERENT EVENTS

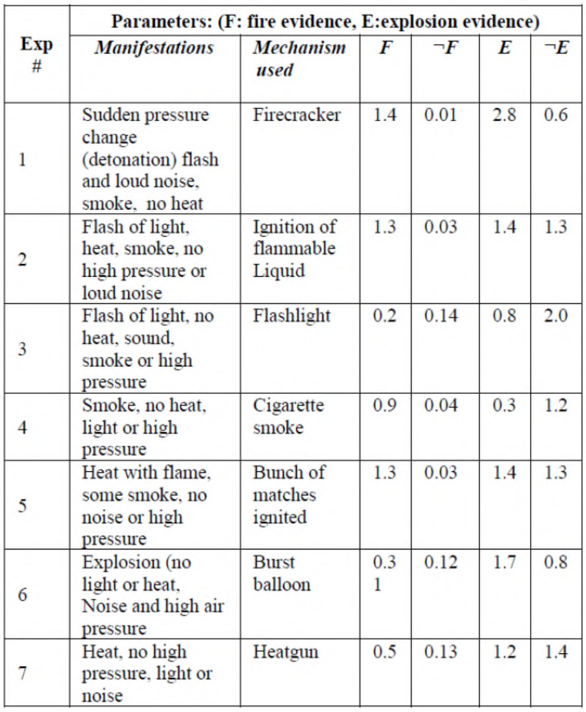

Exp #	**Parameters: (F: fire evidence, E:explosion evidence)**					
	Manifestations	***Mechanism used***	***F***	***¬F***	***E***	***¬E***
1	Sudden pressure change (detonation) flash and loud noise, smoke, no heat	Firecracker	1.4	0.01	2.8	0.6
2	Flash of light, heat, smoke, no high pressure or loud noise	Ignition of flammable Liquid	1.3	0.03	1.4	1.3
3	Flash of light, no heat, sound, smoke or high pressure	Flashlight	0.2	0.14	0.8	2.0
4	Smoke, no heat, light or high pressure	Cigarette smoke	0.9	0.04	0.3	1.2
5	Heat with flame, some smoke, no noise or high pressure	Bunch of matches ignited	1.3	0.03	1.4	1.3
6	Explosion (no light or heat, Noise and high air pressure	Burst balloon	0.31	0.12	1.7	0.8
7	Heat, no high pressure, light or noise	Heatgun	0.5	0.13	1.2	1.4

V. DISCUSSION AND CONCLUSIONS

Our approach implicitly considers sensor reliability in assigning evidence weights to sensor data. An explicit modelling of sensor unreliability would allow additional scenario to be produced. Also, we use crisp thresholds for the detection of manifestations, i.e. a manifestation has either been detected or not. In actuality, the boundaries between a manifestation and a non-manifestation may be fuzzy rather than crisp. For example, the distinction between a bright light and a flash of light may be better defined in terms of membership to a fuzzy set of values. Since LR+ shows how much more likely it is for a truly occurred event to score higher than a non-event, Table III suggests that the above sensor setup is more suitable for detecting explosions rather than fires, while minimising false positive rate. This is both due to the relative assignment of weights to different phenomena and to the types of sensors used for detection. This could indicate that more fire specific detection sensors would need to be deployed to improve sensitivity and specificity.

Another limitation of our approach relates to the need to assign evidence weights to each manifestation per corresponding event. Such weights can be obtained empirically by historical data recorded over long periods (where for example multiple explosion and fire events occurred with their manifestations statistically analysed). Where such data are not available and/or the particular context characteristics must also be accommodated (e.g. the topology/layout of the area where the explosion or fire occurs), expert opinion is necessary,

Amongst the advantages of the proposed approach, we include the clarity of the model and the simplicity of the calculations it employs. This unlike for example, approaches based on neural networks, makes the model easily open to inspections and necessary calibrations. Additionally, since the calculations involved are rather rudimentary, devices of limited computational power and storage can be employed, such as gateways and other 'edge' devices that are physically deployed closer to the sensors.

For further research, our approach could include more sophisticated pattern matching techniques for detecting event manifestations, combination with other machine learning techniques such as neural networks, and integration with intelligent processing and decision support systems used for example, in risk management.

ACKNOWLEDGEMENT

Work described in this paper was financially supported by EU Horizon 2020 Project CHARIOT (Cognitive Heterogeneous Architecture for Industrial IoT- Grant No. 780075).

REFERENCES

[1] B. Khaleghi, A. Khamis, O. Fakhreddine, S. Karray and N. Razavi. “Multisensor data fusion: a review of the state-of-the-art”. Information Fusion. Volume 14 Issue 1, January, 2013 pp. 28-44.

[2] M. Wang, P. Charith, Jayaraman, P. Prem, M. Zhang, P. Strazdins, and R. Ranjan. “City data fusion: sensor data fusion in the internet of things”. International Journal of Distributed Systems and Technologies (IJDST), 2015.

[3] J. Pearl. Probabilistic Reasoning in Intelligent Systems: Networks of Plausible Inference. CA: MKP, 1988.

[4] G. Shafer. A Mathematical Theory of Evidence. Princeton University Press, 1966.

[5] E. Pashaa, H.R. Mostafaeib, M. Khalajc and F. Khalajb “Fault diagnosis of engine using information fusion based on Dempster-Shafer theory”. J. Basic. Appl. Sci. Res., 2(2)1078-1085, 2012.

[6] H. Wu, M. Siegel, R. Stiefelhagen and Yang J. “Sensor fusion using Dempster-Shafer theory”. IEEE Instrumentation and Measurement Technology Conference Anchorage, AK, USA, 21-23 May 2002.

[7] R. Fay, F. Schwenker, C. Thiel and G. Palm. “Hierarchical neural networks utilising Dempster-Shafer evidence theory”. Artificial Neural Networks in Pattern Recognition: Second IAPR Workshop, ANNPR 2006, Ulm, Germany, August 31-September 2, 2006, pp.198-209.

ISBN: 978-1-61208-659-0

Application of Smart City Technology in Aiken, South Carolina

Adam Prey and Jiannan Zhai

Institute for Sensing and Embedded Network Systems Engineering
Florida Atlantic University
Boca Raton, United States
e-mail: aprey2016@fau.edu, jzhai@fau.edu

Abstract— **This paper examines how the city of Aiken, South Carolina implemented Internet of Thing (IoT) devices throughout the city to monitor storm water runoff that had been causing severe erosion in the nearby Hitchcock Woods. The role of the monitoring system is to provide feedback for city planners so that they can better understand the outcome of implemented Green Infrastructure to reduce water runoff. Previously, no monitoring system for water flow had been in place, leaving the results of past efforts to reduce runoff questionable, as data collection had been limited. Using a configurable IoT sensing platform, more data about the water runoff can now be collected. Our paper examines this IoT sensing platform and how it is implanted to make Aiken a smart city.**

Keywords- Internet of Things; IoT; Smart City; Erosion; MoteStack; Storm water management.

I. INTRODUCTION

Over the last 20 years, the cost and size of electronic devices have decreased significantly. During this same time, the capabilities of wireless networks dramatically improved as well. While the Internet of Things as a concept was thought of many years ago, having better wireless networks with smaller and cheaper electronics has finally made it possible. In the early generations of IoT, it was limited to city scale deployments due to the high cost of the technology and infrastructure to run properly. These devices started to become 'smart' by collecting data about their usage they began to automate themselves. With the decrease in the cost, IoT devices entered consumer markets and gained widespread use. Many uses have been found for these technologies, both on consumer and city-wide scales. By integrating smart devices into a city's infrastructure, important city data can be collected, enabling city planners and policy makers to better manage, plan, and protect a city's infrastructure, environment, and economy.

Taking advantage of smart city developments is the city of Aiken, South Carolina. Aiken is home to the Hitchcock Woods, one of the largest urban forests in the United States. Within the Hitchcock Woods there is an ephemeral stream called the Sand River, and as Aiken has grown so has the Sand River. The stream, once small enough that a person could easily step over, has grown to be over 15 feet deep and 70 feet wide over the past 40 years [5]. This rapid growth has been caused by erosion from Aiken's storm water runoff. With the city growing larger, more storm water runoff is sent through a 10-foot pipe at the head of the Sand River causing an increasing flow of water down the Sand River, worsening the erosion of the surrounding forest [10]. This erosion has resulted in extreme damage to the Hitchcock Woods and costs the city of millions [6] of dollars in attempts to control the damage.

An attempt to better manage the runoff was a Green Infrastructure project that took advantage of a sensing infrastructure previously proven as an effective tool for monitoring water conditions at the nearby Savannah River [7, 8]. This configurable end-to-end sensing infrastructure was adopted for the needs of Aiken to measure the effectiveness of their Green Infrastructure developments. It provided a reliable and scalable solution to monitor the environmental conditions of Aiken with real-time data collection, transmission and processing of the data sent directly to environmental scientists, policy makers and engineers of Aiken [12]. The sensor network was configured to collect data on the soil, and water flow throughout the city and watershed [9]. In this paper, we present an analysis of the technology used in Aiken's development as a smart city. In Section 2 is the background detailing other smart city implementations. In Section 3, we review the system architecture's sensing, networking and middleware layers. In Section 4, we conclude our work.

II. BACKGROUND

Over the past few years, numerous cities have begun to integrate sensing networks into their infrastructure. The city of Aarhus, Denmark began a smart city initiative in 2010 with the goal of developing new sensing and networking technologies to better manage the city's water, waste removal and heating services [1]. Aarhus worked with private and public sectors while encouraging volunteers to participate by having the data collected available to the public. With the data being public, several competitions focused on the sensing, networking, and data processing technologies became popular and helped grow the smart city initiative. Through these initiatives and engaging the public with the development of its smart technologies, Aarhus found effective and meaningful ways to improve upon the environmental impact of a large city while enhancing the quality of life of the people living within the city.

The city Kayseri, located in Turkey, served as a testing ground for a smart waste management system [4]. By attaching sensor systems to dumpsters and other waste collection boxes researchers could collect data about waste production. Using this data, the researchers developed a software system that planned optimized routes for garbage collectors and sent these routes directly to the garbage collectors via a cellular network. The implementation of this system reduced the amount of pollution Kayseri produced as garbage collection ran more efficiently and less frequently. The new system also provided the city with 30% cost savings of running garbage collection by reducing the amount of upkeep for the garbage trucks [4].

Smart systems are now used in agriculture as well. These systems commonly use soil sensors to provide farmers valuable data about soil conditions and crop health. In Jojoba, Israel, soil sensors are used to collect real-time data in orchards and other farmlands, allowing farmers to develop irrigation plans for their crops. Machine learning techniques are also applied to the data collected from the soil sensors to build better prediction models for farm irrigation [2]. Soil sensors in agriculture need to be buried deep enough to avoid damage from plowing machines while still having access to power and a means to communicate with the surface and other sensors.

For Aiken's application, a more robust networking solution was put in place by having cellular and Wi-Fi access points than using only one or the other. The Aiken system is also easy to configure allowing for rapid deployment and servicing of the system. The sensing layer is also more sophisticated in that a single node has access to multiple sensors and wirelessly transmits collected data.

III. SYSTEM ARCHITECTURE

As shown in Figure 1, the sensing infrastructure consists of four layers: (i) The sensing layer that uses a wireless sensing platform called MoteStack [3]. (ii) The networking layer, where information collected from the sensing layer is sent to a computing center for data processing. (iii) At the computing center the data is processed through middleware to automate the validation, storage and dissemination of the collected data. (iv) The fourth layer is the front-end used to present the information to end-users.

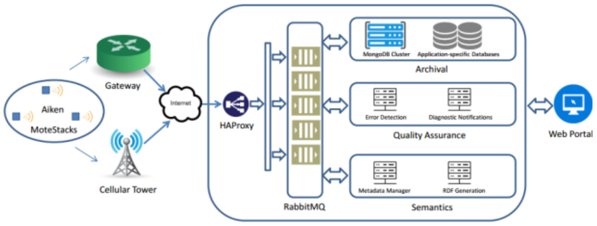

Figure 1. Layered Sensing Infrastructure

A. *Sensing Layer*

The stackable MoteStack sensing platform allows it to be configurable and scalable for many applications. MoteStacks are built from multiple layers of interchangeable circuit boards to perform different tasks. This interchangeability gives the macroscope a high degree of flexibility in its applications. To ensure proper functionality and ease of deployment, the MoteStack includes a Software Stack and purpose built MoteStack Compilation Tool.

(a) Control Board (b) I/O Board

(c) NVSRAM Board (d) Cellular Board

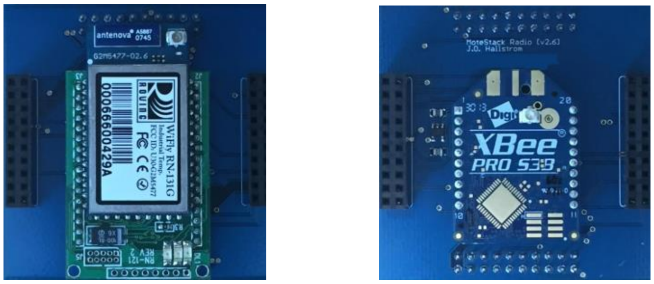

(e) Wi-Fi Board (f) Xbee Board

Figure 2. MoteStack Boards

Figure 2 (a) shows the Atmel ATmega644 microcontroller used in the MoteStack for sensor readings, radio control, and task scheduling. Figure 2(b) shows the I/O and SDI-12 board that handles communication to the sensors over various protocols with on board LED's to indicate system status. The MoteStack includes three RF boards, a XBee RF module Figure 2(f), a Wi-Fi board Figure 2(e), and a cellular board Figure 2 (d) to allow an internet connection at designated base stations. To support non-volatile data logging an NVSRAM board is included in the MoteStack shown in Figure 2(c).

A software driver is developed for each hardware module and can be included in the software as needed. Due to the nature of the embedded systems -- batteries powered and resource constrained, the software designed for the MoteStack focuses on efficiency and reliability. The core of the MoteStack software is an efficient task scheduler. At startup, the drivers for the installed board are initialized and the designed tasks are passed to the task scheduler with parameters used to specify the times when the tasks will be executed. To accurately schedule the tasks, an external crystal with corresponding driver is used to keep track of time.

In the early phase of the project, each MoteStack was configured and programmed by the engineering team and shipped to the field team for deployment. To avoid spending unnecessary time on MoteStack reprogramming and shipment, a tool called MoteStack Compile Tool (MSCT) was developed, allowing the field team to reconfigure and reprogram the MoteStack without the help from the engineering team. The MSCT consists of two components: (i) a server application used to generate executable images for the MoteStacks based on the configurations entered by the end user; and (ii) a desktop application, shown in Figure 3 used to modify MoteStack configurations, download executable images and reprogram the MoteStacks. Once the Compile button on the desktop application Graphical User Interface (GUI) is pressed, the new configurations are sent to the server application that generates a new executable image based on the received configurations. Then, the image is sent to the desktop application that reprograms the connected MoteStack with the downloaded image.

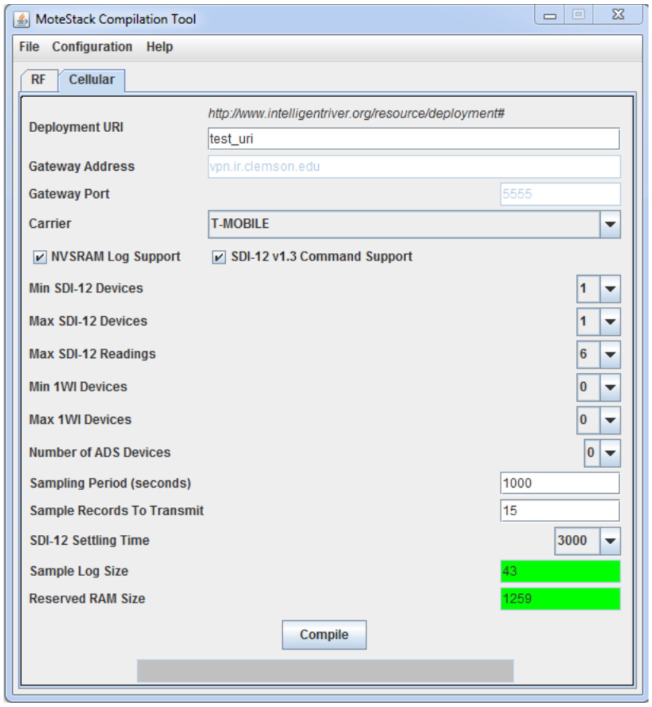

Deployment URI: http://www.intelligentriver.org/resource/deployment# test_uri
Gateway Address: vpn.ir.clemson.edu
Gateway Port: 5555
Carrier: T-MOBILE
☑ NVSRAM Log Support ☑ SDI-12 v1.3 Command Support
Min SDI-12 Devices: 1
Max SDI-12 Devices: 1
Max SDI-12 Readings: 6
Min 1WI Devices: 0
Max 1WI Devices: 0
Number of ADS Devices: 0
Sampling Period (seconds): 1000
Sample Records To Transmit: 15
SDI-12 Settling Time: 3000
Sample Log Size: 43
Reserved RAM Size: 1259

Figure 3. MoteStack Compilation Tool GUI

The MoteStacks are assigned a Unique Resource Identifier (URI) to be used by middleware before deployment. The middleware uses the URI assign the correct metadata for each MoteStack.

The MoteStacks deployed in the city of Aiken uses (i) soil sensors to collect soil temperature, conductivity, and water content at depths of 6, 12 and 18 inches, and (ii) doppler flow sensors to monitor water quality and flow as it moved through the Aiken watershed. These sensors were selected as they could provide city planners a clearer picture of where water off is flowing too and where it is coming from. A total of 20 sensor locations where deployed throughout the major areas of water runoff within Aiken and the Hitchcock Woods. With the developed software tools and configurable design of the MoteStack the field team was able to easily deploy MoteStacks in Aiken.

B. *Networking Layer*

To send messages from the MoteStacks to the back-end, already existing Wi-Fi and cellular infrastructures are used along with Xbee and Wi-Fi meshes for communications. Custom gateways are used to connect the MoteStacks to the Internet. The gateways service all the messages, network maintenance, and monitors system status. In the mesh network, the gateways provide the MoteStacks with base stations to the Internet. The messages collected from the MoteStacks at a gateway are delivered to the back-end middleware. Several gateways include a cellular connection to as a backup connection to the Internet in case of an Internet outage, improving the robustness of the networking layer. A Cellular Signal Tester, shown in Figure 4, was built to test the cellular signal strength of different carriers on each deployment site, based on the signal strength, a carrier is chosen for the deployment.

Figure 4. Cellular Signal Tester

C. Middleware Processing

The middleware stack is a cloud-based virtual machine network hosted on a private multi-server computer infrastructure. This network allows the middleware to be configured, scaled and processes data through three modules, a messaging module, data storage module, and processing module.

A load balancer is used with RabbitMQ for the Advanced Message Queuing Protocol (AMQP) standard. Information from the MoteStacks pass through the load balancer to be distributed to a RabbitMQ cluster consisting of several RabbitMQ nodes. The messages are then sent to a diagnostic or observation queue to be processed. When a message is successfully received an acknowledgement is sent to the MoteStack, if no acknowledgement is received by the MoteStack, it buffers and sends the message again.

The data storage module is dispersed through several virtual machines on different physical to provide improved system scalability and reliability. The data is stored in MongoDB instances with a duplicate instance for storing metadata of the module. A single instance serves as an interface to the storage module.

The processing module consists of consumer programs with access to the diagnostics and observation queues for message processing. Messages are archived in the data storage module to create a log for all received data. Diagnostics messages are archived and sent to a notification program that checks timestamps of the diagnostic messages to verify that the MoteStacks are working normally.

Afterwards, messages from the observation queue are processed. The metadata from the MoteStacks is used to verify received data matches the parameters outlined in the specific MoteStack's metadata. Finally, the metadata is used for processing raw data into more human-readable data and sent back to the messaging module for storage in application specific databases.

IV. CONCLUSION

While the results of Aiken's Green Infrastructure plan show a consistent reduction in the calculated runoff, there was no statistically relevant reduction for the watershed [8, 11]. However, the MoteStacks and their sensing infrastructure allowed for consistent, meaningful data collection before and after the green infrastructure plan was completed. The infrastructure proved to be more than adequate for the demands placed on the system during deployment. The system was reliable and built in redundancies such as having both a Wi-Fi and cellular connection ensured that little data would be lost. This data provided key measurements that evaluated the effectiveness of the changes made by Aiken. Using these smart technologies, the city of Aiken, SC could effectively design and implement a smart city component for itself to aid in the management and control of the city and their water runoff.

REFERENCES

[1] C. Snow, D. Håkonsson, and B. A. Obel, "A Smart City is a Collaborative Community: Lessons From Smart Aarhus" California Management Review, vol. 59, pp. 92-108, Nov. 2016, doi: 10.1177/0008125616683954.

[2] A. Goldstein et al., "Applying machine learning on sensor data for irrigation recommendations: revealing the agronomist's tacit knowledge." Precision Agriculture, vol. 19, pp. 421-444, 2017, doi: 10.1007/s11119-017-9527-4.

[3] J. Zhai et al., "Harnessing the Flow of Ecological Data Across Networks, Middleware, and Applications" IEEE 3rd World Forum on Internet of Things(WF-IoT) pp. 129-134, 2016, doi: 10.1109/WF-IoT.2016.7845411

[4] Z. Oralhan, B. Oralhan, and Y. Yiğit, "Smart City Application: Internet of Things (IoT) Technologies Based Smart Waste Collection Using Data Mining Approach and Ant Colony Optimization." International Arab Journal Of Information Technology, Vol 14, pp. 423-427, Jan. 2017

[5] P. Kent, "Of Seeds and The River", Glimpse, Spring 2012, pp. 14-22Y.

[6] Yorozu, M. Hirano, K. Oka, and Y. Tagawa, "Electron spectroscopy studies on magneto-optical media and plastic substrate interface," IEEE Transl. J. Magn. Japan, vol. 2, pp. 740–741, August 1987 [Digests 9th Annual Conf. Magnetics Japan, p. 301, 1982].

[7] "Sand River Headwaters Green Infrastructure Project" February 2013. Available from http://media.clemson.edu/public/restoration/sand%20river/agi_finalreport_022113-web.pdf retrieved: Jul. 2018

[8] G. W. Eidson, et al., "Sand River Headwaters Green Infrastructure Project, City of Aiken, South Carolina: A collaborative Team Approach to Implementing Green Infrastructure Practices." 2010 South Carolina Water Resources Conference, Oct. 13, 2010.

[9] C. Post et al., "Monitoring spatial and temporal variation of dissolved oxygen and water temperature in the Savannah River using a sensor network." Environmental Monitoring and Assesment May 2018, doi: 10.1007/s10661-018-6646-y.

[10] S. Esswein, J. O. Hallstrom, C. Post, G. Eidson, and D. White, "Augmenting Hydrologic Information Systems with Streaming Water Resource Data" South Carolina Water Resources Conference, Oct 2010.

[11] G. Eidson et al., "The South Carolina Digital Watershed." International Journal of Distrubted Sensor Networks, Jul. 2010, doi: 10.1155/2010/970868

[12] D. White et al., "The Intelligent River©: Implementation of Sensor Web Enablement technologies across three tiers of system architecture: Fabric, middleware, and application" Conference: Collaborative Technologies and Systems, Jun. 2010, doi: 10.1109/CTS.2010.5478493

Azimuth Angle Estimation Using a Dual Accelerometer Vector Sensor with Active and Passive Underwater Signals

Paulo Santos
Paulo Felisberto
and Sérgio M. Jesus

LARSyS
University of Algarve
Campus de Gambelas
8005-139, Faro, PORTUGAL
Email: {pjsantos,pfelis,sjesus}@ualg.pt

Friedrich Zabel

MarSensing Lda
Campus de Gambelas
8005-139 Faro, PORTUGAL
Email: fredz@marsensing.com

Aníbal Matos

INESC TEC
Technology and Science
Porto, PORTUGAL
Email: anibal@fe.up.pt

Abstract—**During decades, the direction of arrival estimation, in terms of azimuth and elevation angles, have been obtained using the pressure acquired with hydrophones or arrays of hydrophones. More recently, the particle velocity information became important in this research area, since the left/right ambiguity can be canceled when Vector Sensors (VS) or VS Arrays (VSA) are used, due to their high spatial directivity. The main objective of this paper is to estimate azimuth angles using a prototype called Dual Accelerometer Vector Sensor (DAVS) with active and passive underwater signals. The DAVS consists of a pressure sensor and two tri-axial accelerometers arranged in a compact unit. The advantage of this equipment is its portability and autonomy. Therefore, it can be easily deployed or embarked in a moving platform. The experimental data results presented in this paper were obtained during the REX'17 experiment where: 1) the DAVS was mounted in an AUV for azimuth angles estimation using active signals and 2) the DAVS was moored in a fixed position collecting passive signals from sources of opportunity. The azimuth estimation results are stable during time, for both active and passive signals, leading to the conclusion that this compact device may be used for platforms self-localization and in operations involving target detection.**

Keywords–Azimuth angle estimation; Vector Sensor signal processing; Intensity based method, Pressure and particle velocity combination.

I. INTRODUCTION

The localization of sources in terms of azimuth and elevation angles estimation has been, traditionally, obtained using hydrophones or arrays of hydrophones. However, the directional information of sound field can be easily obtained using a Vector Sensor (VS). VSs are devices capable of measuring the particle velocity in the three axes and also the pressure, when a hydrophone is collocated. The particle velocity components can be obtained from pressure gradient for each axis or by using tri-axial accelerometers, currently the most common device. The advantage of VS is that it captures more information at a single point of space than a hydrophone, providing high spatial directivity.

Theoretical works involving VS appeared in the 90's, first for sound propagation in the air [1] and then for underwater acoustic sound propagation [2], [3]. The spatial filtering capabilities of VS for Direction of Arrival (DOA) estimation clearly outperforms acoustic pressure only (scalar) hydrophones. The combination of several Vector Sensors in an Array (VSA) can be used to estimate both azimuth and elevation angles, eliminating the well know left/right ambiguity that exists with linear hydrophone arrays [4]. Taking advantage of its directionality and its high performance in DOA estimation, the use of VS became a subject of investigation [5]–[8].

Different methods and different estimators for DOA with arrays of hydrophones and VSs appeared in scientific community [9]–[11], but the DOA can be achieved by using a single vector sensor. Therefore, research on a single VS processing has begun to appear in underwater acoustic applications. The azimuth angle estimation based on an Intensity method using a single VS was published in [12]. This work illustrates the spatial filtering capabilities of a single VS applied to source localization of a known broadband source signal. In order to reduce the complexity of arrays and taking into account the information obtained from a single VS, a Dual Accelerometer Vector Sensor (DAVS) was developed during the framework of the WiMUST European project [13]. The DAVS is a compact sensor, composed of a hydrophone (pressure sensor) and two particle velocity sensors (tri-axial accelerometers) aligned in a vertical axis. This compact sensor allows for easy mounting and operation on Autonomous Underwater Vehicles (AUV's). The use of a dual accelerometer configuration with a single hydrophone was based on previous studies [14]. They showed that, depending on the application, particle velocity can be combined with the pressure with advantage for DOA estimation or with particle velocity difference for bottom characterization improvements. This configuration is already proven to be a good solution for azimuth estimation of active signals when mounted on AUV [15] or for bottom characterization [16]. The novelty of this work is that the azimuth angle estimation is determined for passive signals when DAVS was moored.

The objective of this work is to present results for azimuth angle estimation using active and passive signals for target detection. The experimental data were acquired with the DAVS system during the REX'17 Sea trial. The REX'17 experiment was organized by the Portuguese Navy and was carried out in the area of Lisbon Naval Base (BNL), Alfeite, Portugal, between the 11th and the 13th of July 2017. The DAVS was mounted on the MARES AUV from INESC-TEC, Porto, and acquired signals from a Lubell source for platform self-localization. Moreover, the DAVS was anchored to collect passive signals for detection and to follow “intruders”.

The paper is organized as follows: Section 2 describes the dual accelerometer vector sensor - DAVS system, used in this work; Section 3 makes an overview of the REX’17 experiment setup and the equipment used; Section 4 presents the experimental data analysis for one mission of the MARES AUV trajectory and for one run of a boat passing near the DAVS location, in terms of received and processed signals, presenting the azimuth estimation results and, finally, Section 5 draws conclusions of this work.

II. DAVS - DUAL ACCELEROMETER VECTOR SENSOR

The DAVS system prototype was developed in the framework of the WiMUST European project [13], which aimed to simplify and to improve the efficacy of actual geo-acoustic surveys through the use of AUV’s. Bearing in mind this objective and in order to streamline underwater operations, the DAVS was designed as a compact and portable equipment for underwater parameters estimation, as for example DOA estimation. The simplicity of this system allows it to be easily moored or embarked in mobile platforms such as AUV’s.

(a)

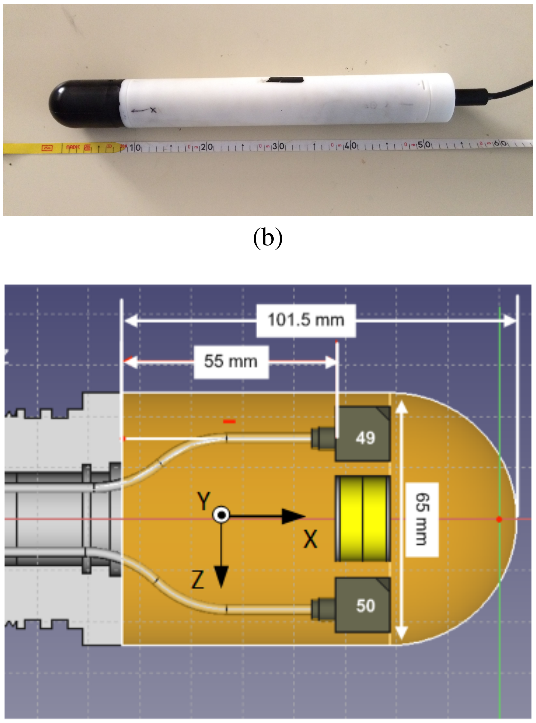

(b)

Figure 1. A photo of the Dual Accelerometer Vector Sensor (DAVS) system (a) and the internal view of the acoustic sensing part (black nose), where it is seen the two accelerometers (gray blocks, numbered as #49 and #50) and the hydrophone (yellow cylindrical) and their position relatively to the Cartesian coordinate system (b). The x-axis is pointing to the front nose, the y-axis is pointing out of the paper and the z-axis is pointing from the #49 to the #50 accelerometer.

Figure 1 (a) shows a photo of the DAVS system where there can be seen two main parts: the acoustic sensing part (black nose) and the container (white tube). The total length of the device is 585 mm and its diameter is 65 mm, having the black nose a length of 101,5 mm, as seen in the photo. The acoustic sensing part is constituted by two tri-axial accelerometers from PCB Piezotronics (gray blocks) and by an in-house built end-cupped cylindrical hydrophone made of PZT piezoelectric material (yellow cylindrical component) between them, as presented in Figure 1 (b). The orientation of the accelerometers components relatively to the Cartesian coordinate system is also shown in the insert, where the x-axis is pointing to the front nose, the y-axis is pointing out of the paper and the z-axis is pointing from the #49 to the #50 accelerometer. The container houses all the electronics, the acquisition system and the batteries. The DAVS system overview, the characteristics of the sensors, the electronic part, the connections, the acquisition system and the power supply are described in detail in [13]. The DAVS system could be powered by batteries, when it is mounted on autonomous mobile platforms, or by cable, when it is not operated autonomously. The cable is also used to connect the DAVS to a portable computer for real-time streaming.

Depending on the application, the dual accelerometer configuration permits that, on one hand, the particle velocity from each accelerometer output could be combined with the pressure for azimuth and elevation angle estimation, or on the other hand, the particle velocity can be combined with the particle velocity difference for bottom characterization improvement [16].

III. REX’17 EXPERIMENTAL SETUP

The REX’17 experiment was organized by the Portuguese Navy in collaboration with the Naval School, where the Naval Base of Alfeite (BNL) facilities in Lisbon were made available for research operations. The objectives of this experiment were to evaluate the DAVS behavior when moored or mounted on the MARES AUV from INESC-TEC, Porto [17], for seabed exploration, bottom characterization and for intruders detection. In this work, it will be presented experimental results for azimuth angle estimation, using active and passive signals.

The operations were conducted in the area of BNL, between 11th and 13th of July, 2017. Figure 2 shows a satellite

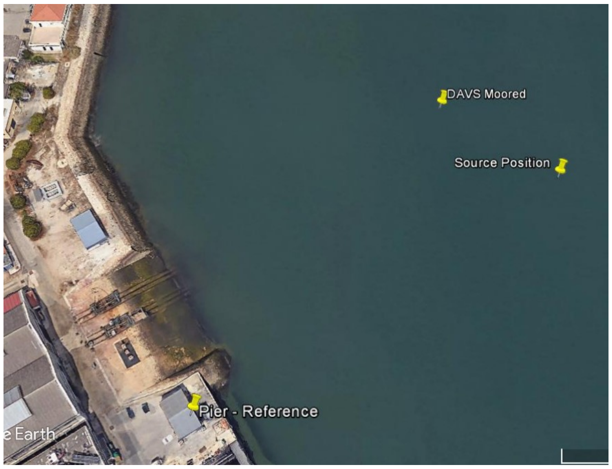

Figure 2. Satellite view of the test area where the location of the acoustic source during event 1 and the DAVS location on event 2, as well as the reference mark in the pier are included.

view of the test area where the location of the source (for active signals transmissions) and the DAVS (when is moored) were included. The mark located on the pier was used as reference (origin of the Cartesian coordinate system) for the positioning and trajectories of the MARES AUV during the experiment. At the source location, it was estimated that the water depth varied approximately from 4.5 m to 6.5 m, while the bathymetry of the area is mostly flat. The experimental data presented herein are related to the events:

1) Event 1 (EV1) dedicated to platform self-localization where the DAVS, mounted beneath the MARES AUV, aquired signals from a sound source moored in a fixed position, as shown in Figure 2;
2) Event 2 (EV2) reserved to port security where the DAVS was moored in a fixed position, acquiring ambient noise produced by boats in the area.

A. Setup for Event 1

During EV1 the DAVS was mounted beneath the MARES AUV, as shown in Figure 3 (a), such that the two accelerometers and the hydrophone were aligned with the vertical z-axis, being the #50 the shallowest accelerometer. The DAVS x-y plane is parallel to the experiment X-Y horizontal plane, where the positive z-axis points upwards and the positive x-axis points to the sailing direction, as drawn in Figure 3 (b).

(a)

(b)

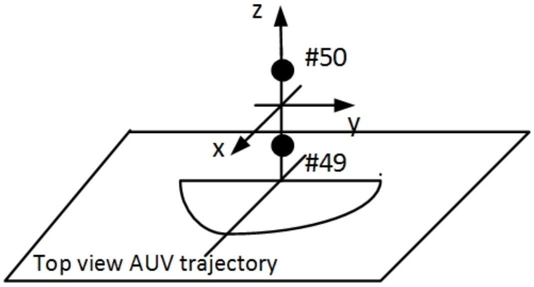

Figure 3. The MARES AUV with the DAVS attached to it in position before deployment (a). Drawing of the DAVS orientation for EV1 when DAVS was AUV mounted with X-Y plane (Top view of AUV trajectory) parallel to the DAVS x-y plane and the accelerometers were aligned with the vertical z-axis, being the #50th the shallowest one (b).

The signals were emitted by a Lubell 916C source, deployed at 3 m (source location in Figure 2) from the bottom in a variable water depth due to tide, ranging from approximately 4.5 m to 6.5 m. The emitted signals were a sequence of Linear Frequency Modulated (LFM) in the 1-3 kHz frequency band, with a time duration of 100 ms followed by 200 ms of silence. In the acquisition, these signals were sampled at 10547 Hz.

B. Setup for Event 2

The objective of EV2 was to test the ability of the DAVS system for DOA estimation to detect and to follow intruders. For this purpose, the DAVS was moored in a fixed position (as shown in Figure 2) and acquired signals at constant height of around 2.5 m from the bottom. In this setup, the x-axis is pointing to the surface and the horizontal plane is defined by the DAVS y-z plane as seen in Figure 4. For this event, the DAVS was powered by cable and the signals were sampled at 52734 Hz.

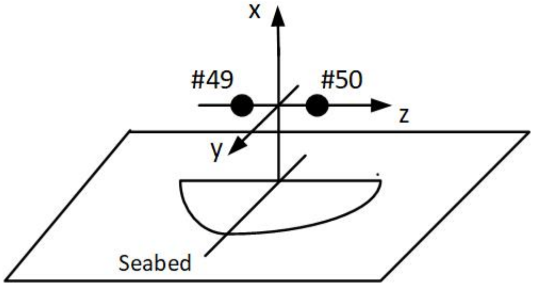

Figure 4. Drawing of the DAVS orientation for EV2 when the DAVS was moored with x-axis pointing upward and the accelerometers were in the horizontal plane parallel to the DAVS y-z plane.

IV. EXPERIMENTAL DATA ANALYSIS

This section presents the azimuth angle estimation obtained with the DAVS, considering active and passive signals. The azimuth angle was evaluated using the Intensity based estimator described in [12]. The processing steps are as follows:

1) the acceleration components (three for each accelerometer) were converted to their respective pressure equivalent particle velocity component, first by using the Fourier Transform to frequency domain (ω), and then by using:

$$\hat{V}_i(\omega) = \frac{\rho}{jk} A_i(\omega) = \frac{\rho c}{j\omega} A_i(\omega), \tag{1}$$

where $\hat{V}_i(\omega)$ is the pressure equivalent particle velocity component, $A_i(\omega)$ is the acceleration component being $i = x, y$ or z-axis, $k = \frac{\omega}{c}$ is the wavenumber, c is the water sound speed, ρ is the water density and ρc is the scaling factor according to the definition of acoustic impedance;
2) back to time domain, the Intensity estimator is applied [12], where the pressure $p(t)$ is cross-correlated at lag 0 with $v_x(t)$ and with the $v_y(t)$ particle velocity components. Then, an estimation of the azimuthal direction of the source signal, Θ_S at large signal to noise ratio (SNR) is given by:

$$\hat{\Theta}_S = \arctan 2 \frac{\langle v_y(t)p(t)\rangle}{\langle v_x(t)p(t)\rangle}, \qquad (2)$$

where $\langle\rangle$ stands for time averaging.

A. Azimuth angle estimation with active signals - EV1

Event 1 was dedicated to acquire data to estimate the azimuth angle for self-localization. The MARES AUV, with the DAVS mounted (see Figure 3 (a)), executes several paths navigating near the surface at a constant depth of $\approx$1.2 m, to cover an area near the source.

Figure 5 refers to the trajectory of the MARES during EV1, with an insert showing the DAVS tri-axial system for an easy observation. The red, yellow, green, cyan and magenta paths corresponds to the time evolution sequence of almost 10 minutes of DAVS' acquired data, each path corresponds to 2 minutes of data. As it can be seen, this trajectory is complex since it has several turns, making it a difficult task for azimuth estimation.

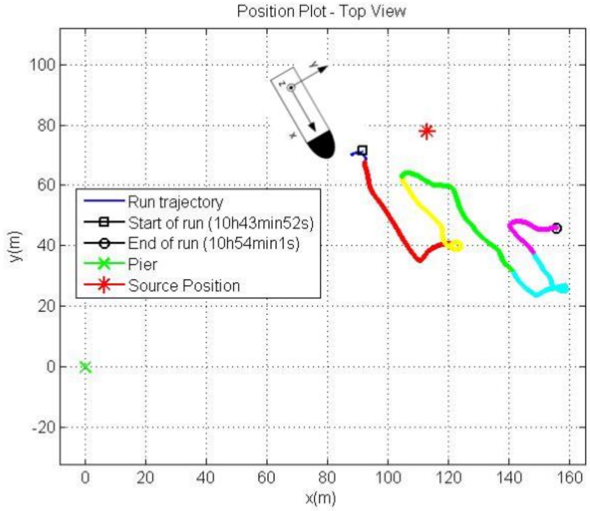

Figure 5. Top view of MARES AUV trajectory relative to the pier position at the origin of the coordinate system, marked by green cross and the source position marked by red asterisk, with the DAVS tri-axial system insert. The red, yellow, green, cyan and magenta paths of trajectory corresponds to the time evolution sequence and each color corresponds at 2 minutes of data for an easy observation.

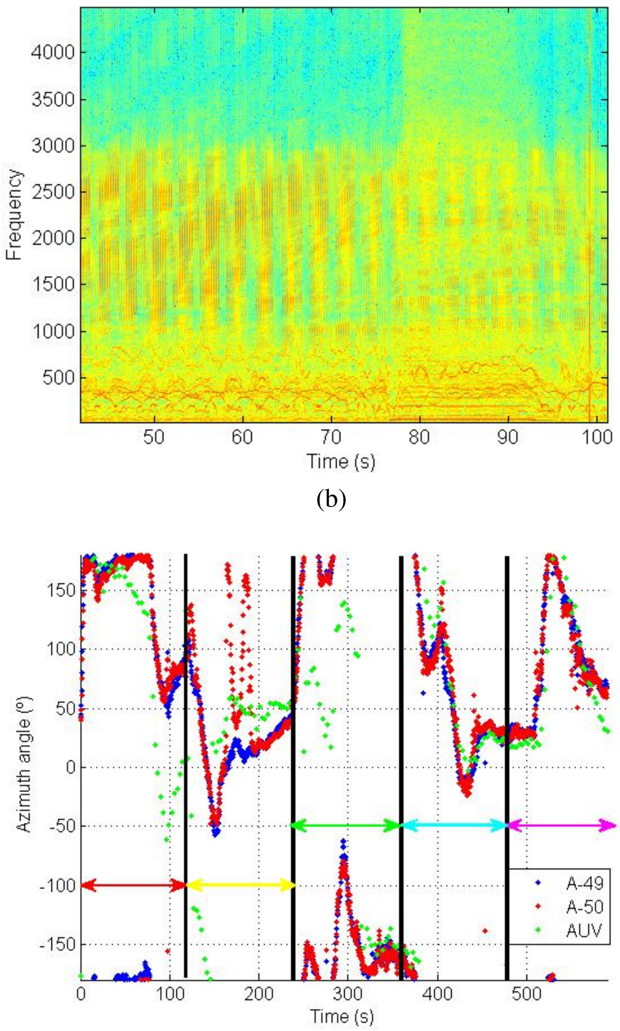

(a)

(b)

Figure 6. Spectrogram of the received signal on the pressure sensor of DAVS for the red path of Figure 5 (a) and the estimation of the azimuth angle between the source and the MARES AUV obtained for both accelerometers (blue dots for #49 and red dots for #50) with the heading angle (green dots, considered the ground truth) for the total duration of the trajectory, around 10 minutes (b). The red, yellow, green, cyan and magenta arrows of plot (b) corresponds to the paths of Figure 5 with a color matching to facilitate the analysis.

Figure 6 (a) shows the spectrogram of part of the signal received on the pressure sensor of DAVS for the beginning of this trajectory (red path). There can be seen the LFM signals, emitted by the Lubell source, in the 1-3 kHz frequency band and also the thruster's noise produced by the MARES AUV for frequencies bellow 1 kHz, out of the signal frequency band. Moreover, it can be clearly seen that the thruster's noise level increases, spreading in the signal band around 80 s, due to the sharp curve in the red path of the trajectory.

The azimuth angle estimation results for this event were obtained using (2), with an integration time of 300 ms, and are presented in Figure 6 (b). As observed, the azimuth angle estimations from both accelerometers (blue dots for #49 and red dots for #50) are inline and they compare almost the time with the green dots, obtained from the heading DAVS's compass data (considered the ground truth). The exception take place when the MARES AUV was coming to the surface (end of red path and begin of green path), where some variability on the heading angle appeared due to the compass are not in the horizontal. Then, the projections are differents, producing the difference between the green dots and the blue and red dots (estimated from (2)). Despite this, in general, the results are in line with the trajectory observed in Figure 5. For an easy analysis of the results, the vertical bars divide the plot in 5 temporal groups, corresponding to the 5 paths of the trajectory with a color matching. The various turns are detected in the results, for example, around 80 s the DAVS is moving away from the source with an azimuth of around 180°. Then, it executes the first curve (in the red path) reducing the angle to almost 50°. Another example is the turn in the cyan path, around 400 s, converging in a straight run, when the MARES AUV approaches the source at the end of cyan path and the beginning of magenta path. In this case, the azimuth angles change from 100° to around -10° and then to 20°, remaining constant. The estimates from both accelerometers are coincident and they match the green dots (given by the heading DAVS's compass data), as seen in Figure 6 (b). From these results, it can be concluded that the DAVS has a high directivity even in motion. The azimuth angles of arrival are detected during long periods of time and the thruster's noise does not influence or disturb the stability of the estimation results, proving that this compact device is useful for self-localization even in curves.

B. *Azimuth angle estimation with passive signals - EV2*

The Event 2 was devoted to acquire signals from sources of opportunity for port security and "intruders" detection. Since in this event the horizontal plane is defined by y-z plane, as shown in Figure 4, equation (2) was rewritten by changing v_x and v_y by v_y and v_z, accordingly. Figure 7 shows the spectrogram of the received signal, on the pressure sensor of DAVS, from noise produced by a boat passing near the DAVS location. It can be seen that the boat passes two times near the DAVS. After 60 s, the signal is more intense since the boat is over the location of the DAVS.

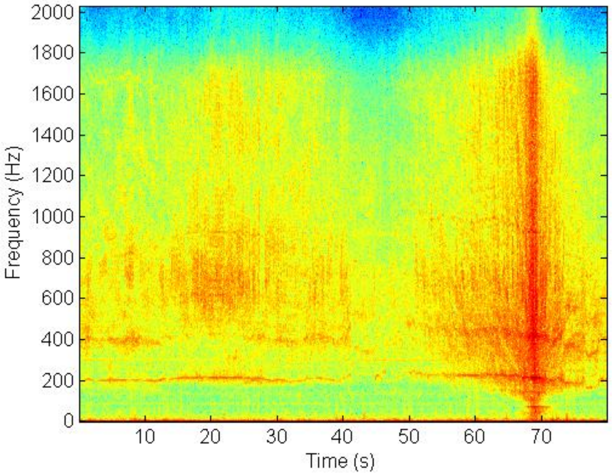

Figure 7. Spectrogram of the received signal on the pressure sensor of DAVS for part of time duration when the signal is detected.

Figure 8 (a) shows a satellite view of the area where the DAVS is moored with one boat's run. It can be seen that the boat passes one time near the DAVS location (on the left), then goes around and approaches the DAVS location from south, passing over it. The respective estimation of the azimuth angle for the run presented in plot (a) is shown in Figure 8 (b). Since the horizontal plane are defined by y-z plane, the blue dots follow the trajectory, beginning and ending at the same value, around 50°. The azimuth angle changes from 50°, increasing to 180° and then from -180° to zero. At the end of the run, the azimuth changes from 0°, when the boat is over the DAVS location, to positive angles (first quadrant), confirming the boat's trajectory. Due to (perhaps) the DAVS is not in the vertical, there are differences between the results from both accelerometers #49 (blue dots) to #50 (red dots), mainly at the beginning, that remain constant in time. However, the results are almost inline with the inserted y and z components orientation in Figure 8 (a), taking into account that the heading of the DAVS compass marked 330° (the z component was assumed the origin of the heading). Although, the SNR is low (where additive rather than multiplicative methods should be used), the DAVS is able to follow the trajectory of the boat proving the utility of this device also for passive signals detection. These results show that the DAVS could be useful for a real-time port security, where the detection and tracking of "intruders" are relevant.

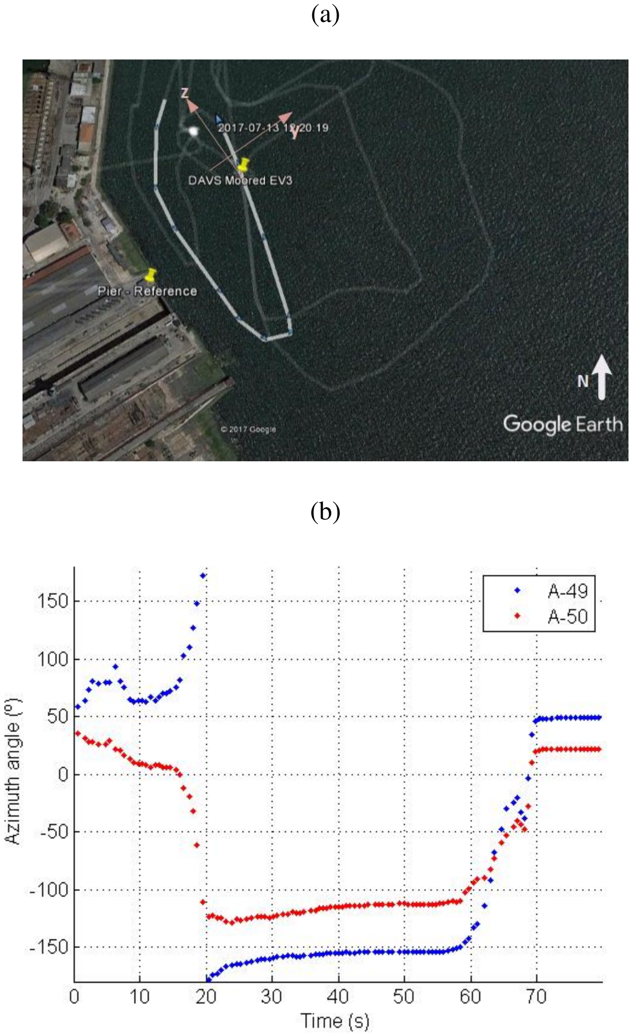
(a)

(b)

Figure 8. Satellite view of the test area with the position of the DAVS moored with one boat's runs near it (a) and the estimation of the azimuth angle for the noise produced by the boat passing near the DAVS for the respective run (b). These estimation were obtained for both accelerometers (blue dots for #49 and red dots for #50) for 80 s of time duration.

V. CONCLUSION

This paper describes, with experimental data, the utility and advantage of a built-in house prototype called Dual Accelerometer Vector Sensor for azimuth angle estimation. This device was designed to contribute for bottom characterization during the framework of WiMUST EU project. However, due to its simplicity and compactness, it can contribute to a quick answer on azimuth estimation, with advantage for self-localization or for noise (passive) signals detection.

The experimental data used in this work were acquired by the DAVS during the REX experiment 2017. The objective of this experiment was to evaluated the DAVS directivity when it was in motion or anchored, for self-localization or port security respectively.

The evaluation of the DAVS directivity in motion was achieved when the DAVS was mounted on the MARES AUV, from INESC-TEC, Porto, while signals in the 1-3 kHz band were emitted by the Lubell source deployed at 3.0 m height from bottom. The experimental results on the estimation of azimuth angle for one mission of 10 minutes were analyzed and these estimates are very stable, equal for both accelerometers and in line with the heading DAVS's compass data, considered the ground truth. Furthermore, they compare favorably the MARES AUV trajectory, even in the several turns where the level of thruster's noise increases.

Moreover, the DAVS was moored, acquiring noise signals produced by boats near the DAVS location in order to estimate the azimuth angle of arrival of sources of opportunity. Although, the SNR is low and the characteristics of the signals are unknown, the results showed that the DAVS has advantage in real-time detection and tracking "the intruders" for port security. The use of different methods and different approaches (like additive methods), which combine pressure and particle velocity for azimuth estimation with passive signals, is the subject of ongoing research work. The characterization of the noise in terms of direction of arrival for different frequencies it will be the next step.

ACKNOWLEDGMENT

The authors would like to thank INESC-TEC, Porto, for the use of the MARES AUV and providing assistance in the AUV's data. The authors also thank the Portuguese navy for making available the Naval Base of Alfeite facilities for research operations and thank the support of H2020 project WiMUST/645141, for providing the DAVS receiver. This work was supported by FCT project UID/EEA/50009/2013.

REFERENCES

[1] A. Nehorai and E. Paldi, "Vector-sensor array processing for electromagnetic source localization," IEEE Trans. Signal Processing, vol. 42, no. 2, February 1994, pp. 376–398.

[2] ——, "Acoustic vector-sensor array processing," IEEE Transaction on Signal Processing, vol. 42, no. 9, September 1994, pp. 2481–2491.

[3] M. Hawkes and A. Nehorai, "Acoustic vector-sensor beamforming and capon direction estimation," IEEE Trans. Signal Processing, vol. 46, no. 9, September 1998, pp. 2291–2304.

[4] C. Wan, A. Kong, and C. Liu, "A comparative study of DOA estimation using vector/gradient sensors," in Proceedings of Oceans06, Asia, Pacific, May 16–19 2007, pp. 1–4.

[5] J. C. Shipps and B. M. Abraham, "The use of vector sensors for underwater port and waterway security," in Proceedings of Sensors for Industry conference, New Orleans, Louisiana, USA, January 27–29 2004, pp. 41–44.

[6] K. M. Krishna and G. V. Anand, "Narrowband detection of acoustic source in shallow ocean using vector sensor array," in Proceedings of Oceans 2009 MTS/IEEE, Biloxi,USA, 2009, pp. 1–8.

[7] P. Santos, P. Felisberto, and S. M. Jesus, "Vector sensor array in underwater acoustic applications," in Proceedings of DoCEIS 10, Doctoral Conference on Computing, Electrical and Industrial Systems, L. Camarinha-Matos, P. Pereira, and L. Ribeiro, Eds., vol. 314. Caparica, Lisbon, Portugal: Springer Boston, February 22–24 2010, pp. 316–323.

[8] P. Felisberto, P. Santos, and S. M. Jesus, "Traking source azimuth using a single vector sensor," in Proceedings of 4th Int. Conference on Sensor Technologies and Applications, Venice, Italy, July 2010, pp. 416–421.

[9] S. Miron, N. L. Bihan, and J. I. Mars, "Vector-sensor MUSIC for polarized seismic sources localization," EURASIP J. Appl. Signal Process., vol. 2005, January 2005, pp. 74–84.

[10] V. N. Hari, G. V. Anand, A. B. Premkumar, and A. S. Madhukumar, "Underwatyer signal detection in partially known ocean using short acoustic vector sensor array," in Proceedings of Oceans 11 IEEE/OES Santander Conference. Santander, Spain: IEEE, June 6–9 2011, pp. 1–9.

[11] K. N. Ramamohan, M. Coutinho, S. P. Chepuri, D. F. Comesaña, and G. Leus, "DOA estimation and beamforming using spatially undersampled AVS arrays," in Proceedings of IEEE International Workshop on Computational Advances in Multi-Sensor Adaptive Processing. CAMSAP'17, December 10–13 2017.

[12] P. Felisberto, O. C. Rodríguez, P. Santos, E. Ey, and S. M. Jesus, "Experimental results of underwater cooperative source localization using a single acoustic vector sensor," Sensors, vol. 13, no. 7, July 2013, pp. 8856–8878.

[13] A. Mantouka, P. Felisberto, P. Santos, F. Zabel, M. Saleiro, S. M. Jesus, and L. Sebastião, "Development and testing of a dual accelerometer vector sensor for auv acoustic surveys," Sensors, vol. 17, no. 1328, 2017, pp. 1–12.

[14] P. Felisberto, P. Santos, and S. M. Jesus, "Acoustic pressure and particle velocity for spatial filtering of bottom arrivals," IEEE Journal of Oceanic Engineering, vol. online, March 2018, pp. 1–14.

[15] P. Santos, P. Felisberto, F. Zabel, S. M. Jesus, and L. Sebastião, "Dual accelerometer vector sensor mounted on an auv - experimental results," in Proceedings of Meetings on Acoustics (POMA), vol. 30. Acoustical Society of America, 2017, p. 0055011.

[16] ——, "Testing of the dual accelerometer vector sensor mounted on an autonomous underwater vehicle," in Proceedings of 4th International Underwater Acoustics Conference and Exhibition. UACE'17, September 3–8 2017.

[17] P. Ramos, N. Cruz, and A. Matos, "The MARES AUV, a modular autonomous robot for environment sampling," http://repositorio.inesctec.pt/handle/123456789/5004, last accessed July, 2018.

Early Prediction of Hypoxia Based on Vitals Analysis and Predictive Analytics

Vahram Mouradian, Afarin Famili, Mahdieh Ashiani
Sensogram Technologies Inc.
Plano, Texas, USA
emails: {vahram, afarin, mahdieh}@sensogram.com

Alexandra Kozhemiakina
Sensogram Technologies Inc.
Kiev, Ukraine
email: alexandra@sensogram.com

Abstract — **This study investigates the SensoSCAN device for both its health monitoring properties and prediction of different diseases by vital sign analysis. The study's objective is to develop a probabilistic model for predicting the presence of hypoxia using correlation chains to assess patients' vital signs gathered by the SensoSCAN. Vital signs, including heart rate, oxygen saturation, activity level, and systolic and diastolic blood pressure, are used to monitor patients' health conditions. Our functional system helps predict hypoxia in its early stages, when distinctive symptoms are absent and patients may not be aware of the presence of the disease. Analysis is made using dependencies in correlation matrix, constructed correlation chains, and predictive analytics. This study utilizes the hypothesis that hypoxia is an effect of consecutive process of activity where the increase in heart rate and respiration rate correlate with a decrease in oxygen saturation. The ultimate goal is to use mathematical Markov processes and build Markov chains, where elevated heart rate and respiration rate and depressed oxygen saturation are caused by higher activity levels. Alternatively, Markov chains are constituted considering other vitals (either heart rate, respiration rate or oxygen saturation) as independent variables. This system will ultimately assist doctors in assessing patients' health by defining the main dependencies between human vitals.**

Keywords-Vitals; hypoxia; SensoSCAN; correlation analysis; predictive modeling.

I. INTRODUCTION

A. *Introduction to Hypoxia*

Oxygen is essential for the development and growth of multi-cellular organisms. Many sophisticated biological mechanisms that involve capturing, binding, and transporting of oxygen maintain our cell and tissue homeostasis [1]. Two terms are used for oxygen deficiency: hypoxia and hypoxemia. Hypoxemia is a frequent cause of hypoxia. They are interrelated as both terms are states of oxygen deficiency; hypoxemia is a condition when there is a significant drop in blood oxygenation and arterial oxygen tension is below normal, while hypoxia is oxygen deficiency on the cellular or tissue level. The lack of treatment of hypoxemia can lead to hypoxia [2][3]. Types of hypoxia include: hypoxic hypoxia (oxygen deficiency in the lungs from high altitude or decreased oxygen saturation (SPO_2) in the air) anemic hypoxia (inability of the blood to accept oxygen in suitable volume), stagnant hypoxia (inability of cells to accept or use oxygen molecules), and histotoxic hypoxia (inability of cells to use oxygen [3][4]). Hypoxemia and/or hypoxia can result in severe changes in cellular metabolism. In the case of oxygen insufficiency, normal metabolism turns to anaerobic metabolism that produces fewer molecules of energy (adenosine triphosphate). Products of this type of metabolism can destroy cell membranes and lead to cell death and organ failure [3][5]. Clinical assessment of oxygen is usually invasive, and a challenging task to tackle. Patients with cardiac and respiratory illnesses, and patients who smoke, consume alcohol, or coffee are in the risk zone. Early recognition, prediction, prevention, and treatment of hypoxemia is very important for patients as the disease can result in decreasing tissue oxygen consumption and severe physiological symptoms as organs begin to fail. Nevertheless, the prediction should be made to prevent many adverse situations [3][4]. Vitals monitoring can help in prediction of the early stages of hypoxia; decreased oxygenation results in abnormalities that include tachycardia (heart rate more than 100 beats per minute (bpm)), tachypnea, (respiratory rate more than twenty-four breaths per minute (brpm)) and high blood pressure. Bradycardia and hypotension are the result of severe hypoxia [3]. The most logical technique for recognition of hypoxia is reading the percentage of hemoglobin that is saturated with oxygen. Normal oxygen saturation is greater than 95%, whereas 90% and below is connected with hypoxemia. The interval between 90% and 95% is considered to be an asymptomatic first stage of the disease that causes confusion. A patient may not be aware of the presence of the disease. Critical stage of the disease, where SPO_2 is 70% or less, may result in brain damage and death. Patients are almost incapacitated, lose consciousness, and stop breathing; their tissues are not provided with an adequate amount of oxygen, resulting in widespread tissue necrosis and organ damage that may not be fully reversible [3][4].

B. *Remote Monitoring Systems and Wearable Devices*

The traditional hospital treatment model keeps patients in hospital beds attached to smart monitoring systems for health assessment. In modern healthcare, wireless sensors and smart technologies make it possible to monitor patients' health parameters under remote oversight of a doctor and can give the ability to effectively monitor health. The accurate and early prediction of clinical events is an important part of remote health-monitoring. Continuous remote health monitoring being established is crucial as it can reduce the staggering cost of observations as wearable sensors are available at a very low cost. Such systems also give the ability to save patient waiting time, and solve the problem with the limited capacity of hospitals. In addition, there is a possibility to control patients' health at any time, from any place [6]. Unfortunately, most remote wearable prediction systems work only on one vital parameter (such as a pulse oximeter that measures a person's SPO_2). As a result, a device that monitors multiple vitals simultaneously can more accurately predict a clinical condition than one that relies on one vital statistic alone)

C. General Information about SensoSCAN

Living tissue is a series of sub-tissues with different concatenations of absorbing optical segments. Each time a pressure pulse reaches the illuminated segment, an increase of the local blood volume occurs, supplements the local absorption, and decreases the light intensity. This model is based on measuring light absorption changes and it is the main model of measuring the blood flow and different vitals in SensoSCAN.

SensoSCAN is a non-invasive wireless wearable mobile device that allows real-time, continuous, remote monitoring and analysis of vital signs. The device works based on an assessment technique, which provides a waveform illustration of pulsatile blood flow. Light is more strongly absorbed by blood than the surrounding tissues, so that the changes in blood flow can be detected by sensor as changes in the intensity of light and provide information on the cardiovascular system of a patient. Advantages of this method include easy set-up, simple and widespread use, low cost, and the ability to take measurements without direct skin contact. The system consists of both photodiode and dual LED emitter as SensoSCAN requires a bi-wavelength light source for vitals measuring. Both red and infrared wavelengths are used as light sources because in this way differences between oxyhemoglobin (HbO_2) and reduced hemoglobin (Hb) with different absorption wavelengths can be assessed for oxygen saturation measurements. Photodiode (PD PIN-8.0-CSL) is used in combination with the dual emitter (DLED-660/905-CSL-3 (a 660nm (red) LED and a companion IR LED with 905 nm)). The device works in conjunction with iOS and Android smartphones and tablets to monitor, share and analyze the data. The captured data is transmitted via Bluetooth Low Energy (BLE) to the smartphone or tablet, which display the parameters. The SensoSCAN application also allows the user to send the data to a dedicated secured cloud system that is accessible via the SensoSCAN web portal.

The system setup is illustrated in Figure 1. The SensoSCAN Monitoring System is intended for use by clinicians and medically qualified personnel to simultaneously monitor multiple vital signs.

SensoSCAN is capable of non-invasive measurement of Respiration Rate (RR), Heart Rate (HR), Systolic and Diastolic Blood Pressure (Systolic BP, Diastolic BP) and Oxygen Saturation of Arterial Hemoglobin (SPO_2), Pulse Rate (PR), and skin Temperature (TEMP) in hospital-based facilities. Vitals are computed based on assessing different features of patients' blood flow (e.g., pulse amplitudes, forms, frequency and analyzing derivatives of the signal etc.). As a result, there is a complex assessment of patients' blood flow, cardiovascular and breathing systems. All these vitals can be used to detect different clinical events and diseases. Using the existing correlations between the vital parameters and their dependencies can help predict severe conditions in their early stages. SensoSCAN is on its final stage of development and becoming a commercially available device. Currently, the device is used for in-house clinical testing, data acquisition and algorithm development.

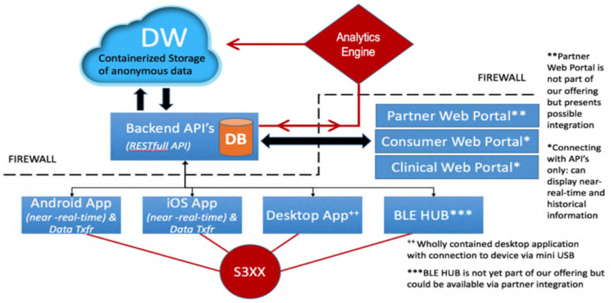

Figure 1. SensoSCAN Measurement System

In the rest of this paper, Section II describes the data acquisition process and the utilized statistical techniques to assess clinical conditions. Section III includes the achieved preliminary results from the subject pool introduced in Section II. Section IV concludes the results at hand. Finally, Section V discusses the shortcomings of the current analysis and our planned path forward.

II. MATERIALS AND METHODS

A. Experimental Design

- Vital Changes Induced by Activity

Four healthy subjects with mean age 25 years (age range 23-26), with a mean heart rate of 72 bpm were recruited. SensoSCAN was used for continuous vitals monitoring. Subjects were advised to be at steady state for 5 minutes, followed by a 10-minute interval activity (while keeping the sensor still on their finger), and the last 5 minutes at rest. Data acquisition took around 20 minutes for each subject.

- Vital Changes by Lowering the Amount of Oxygen

Experiments were run on 10 subjects at a clinical lab in Louisville, CO after approval from the Institutional Review Board (IRB). Test subjects provided their written consent to participate in the study and had the right to leave at any time. The study was conducted by clinical staff in the clinical lab environment where subjects lay reclined. Sensors were placed on subject's finger to collect vitals data. Subjects were given medical grade mixtures of oxygen and nitrogen to induce various hypoxic levels in them. SpO2 levels were brought down to about 70% by inducing more nitrogen via a breathing mask.

B. Vitals Pairwise Correlation

Future dangerous clinical conditions could be predicted by examining the correlation between vital parameters. To this end, Pearson Correlation Coefficient was examined between the pairs of vitals, aiming at predicting a clinical condition such as hypoxia. We computed the Pearson Correlation Coefficient (1) between vital pairs using [7]:

$$r_{xy} = \frac{cov(x,y)}{\sqrt{var(x).var(y)}}, (1)$$

where x and y are the two variables between which Correlation Coefficient (e.g., the two variables could be HR and RR) is computed. Cov(x,y) is sample covariance of the two variables, while var(x) and var(y) are sample variance of variables x and y respectively. The Pearson Correlation measures the strength and direction of linear relationship between two variables. A higher, more positive correlation indicates a strong, direct linear relationship between two variables, while a more negative Pearson Correlation represents the strong, inverse linear association between the two variables. In order to prove the statistical significance of the correlations, the p-value associated with each score is also computed.

C. Correlation Chains in Predicting Hypoxia

The goal is to predict hypoxia from the existing correlations between the vitals. HR, RR, and SPO2 are the most relevant vitals recorded by SensoSCAN in predicting respiratory disease. Elevated HR and RR, accompanied by depressed SPO2 levels are expected in patients suffering from hypoxia. As a result, in order to pre-diagnose hypoxia, correlation chains were generated based on the correlations between the three aforementioned vitals.

III. PRELIMINARY RESULTS

A. Vital Changes Induced by Activity

Pearson Correlation Coefficients between the vital pairs were computed and stored them in a 6 × 6 correlation matrix (Figure 2). Each cell of the correlation matrix indicates the strength of the association between respective vital pairs. The cell color indicates the strength and direction of the association between two parameters. Dark blue indicates the strong, positive correlation between vital pairs. The strong, inverse association between the vital pairs is further indicated with lighter colors (e.g., yellow indicates the strongest inverse correlation between the corresponding variables). TABLE I includes the numerical values of the scores associated with each color-coded cell of the adjacency matrix. As shown in this table, subject's heart beats faster and she breathes faster. This is indicated by the relatively strong, positive Pearson Correlation with magnitude 0.60 ($p < 0.01$) between HR and RR. The inverse, strong Correlation between SPO2 and either HR (-0.63, $p < 0.01$) and RR (-0.49, $p < 0.01$) is also observed in the presence of the interval activity.

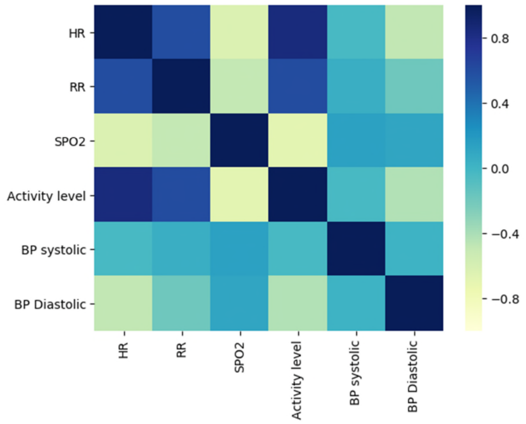

Figure 2. Correlation matrix containing vital pairs Pearson Correlation Coefficients

Considering the strongest correlations and setting a threshold correlation score of 0.5 (the probability due to chance in bivariate analysis), correlation chains between these vitals were constructed. The chain in Figure 3A is generated based on the correlation matrix in Figure 2. The pairwise associations between these vitals (SPO2, HR and RR) is indicative of hypoxia (Figure 3A), while signs of hypoxia are absent in the subject shown in Figure 3B as one of the correlation scores in the correlation chain is below the specified threshold and is not considered significant.

B. Vital Changes Induced by Lowering Oxygen Levels

Correlation matrices (between HR, RR and SPO2) were generated for experiments performed at the clinical lab. TABLE II (the following page) indicates the pairwise correlation results in a subject. As observed, SPO2 has a strong, inverse association with HR ($r = -0.78$, $p < 0.01$); meaning HR increases as the amount of oxygen applied in the mask decreases. This holds true for a weaker inverse correlation between SPO2 and RR ($r = -0.41$, $p < 0.01$), while HR and RR are positively correlated ($r = 0.56$, $p < 0.01$).

C. Predicting Hypoxia from Vital Chain Correlations

Upon reducing and elevating oxygen levels via the breathing mask at the clinical lab, correlations between HR, RR, and SPO2 indicated the presence of hypoxia. The provided correlation chain in Figure 4 shows the resulting chain with the specified correlation scores in one of the participants. Out of 10 subjects participating in this study, 4 happened to be diagnosed with hypoxia based on the developed algorithm.

IV. CONCLUSION AND FUTURE WORK

This work shows a correlation engine capable of predicting hypoxia based on pairwise correlations between vitals. Integration of this engine in SensoSCAN provides health care professionals with a tool, measuring continuous-valued vitals data, which can help them make more educated decisions while diagnosing the patients and advance home-based remote monitoring systems.

TABLE I. PEARSON CORRELATION COEFFICIENT SCORES BETWEEN SIX VITAL PAIRS

	HR	RR	SPO2	Activity	SBP	DBP
HR	1.00	0.60	-0.63	0.85	-0.54	-0.57
RR	0.60	1.00	-0.49	0.61	-0.46	-0.47
SPO2	-0.63	-0.49	1.00	-0.68	0.74	0.75
Activity	0.85	0.61	-0.68	1.00	-0.64	-0.67
SBP	-0.54	-0.46	0.74	-0.64	1.00	0.98
DBP	-0.57	-0.47	0.75	-0.67	0.98	1.00

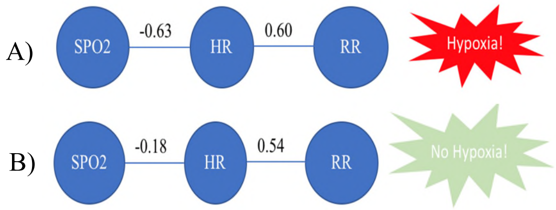

Figure 3. Generated correlation chains indicating the presence (A) and absence (B) of hypoxia

A shortcoming of this method was the limited number of resources due to the invasiveness of the method (as oxygen levels were decreased by inducing more nitrogen via the breathing mask). As a part of the ongoing work, more subjects from varying age groups will be recruited in order to better validate the algorithm. Furthermore, the correlation engine design is ultimately aimed at developing dynamic machine learning algorithms such as Hidden Markov Models [8], taking advantage of Markov chains features to develop probabilistic models that are capable of diagnosing not only hypoxia, but other dangerous clinical conditions such as chronic obstructive pulmonary disease (COPD) and diseases related to the cardiovascular system. The model will ultimately be deployed in the device for remote-monitoring. Prototyping and experimental evaluation will further be implemented in the system in order to generate real-time estimation of chronic diseases with a remarkable accuracy. This is a work in progress and the validity of the hypothesis in diagnosing dangerous clinical conditions by continuous vitals monitoring is under scrutiny.

TABLE II. PEARSON'S CORRELATION COEFFICIENT SCORES BETWEEN PAIRS OF HR, RR AND SPO2

	HR	RR	SpO2
HR	1.00	0.56	-0.78
RR	0.56	1.00	-0.41
SpO2	-0.78	-0.41	1.00

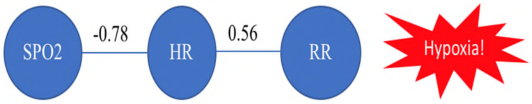

Figure 4. Generated correlation chains indicating the presence of hypoxia based on vitals chains

REFERENCES

[1] A.J. Giaccia, M. C. Simon, and R. Johnson, "The biology of hypoxia: the role of oxygen sensing in development, normal function, and disease", Genres & Development 18 2004 Sep 15, 18(18), pp.2183–2194, https://doi.org/10.1101/gad.1243304.

[2] T. Meštrović, "What is hypoxemia?" [Online] Available from: https://www.news-medical.net/health/What-is-Hypoxemia.aspx [retrieved: July, 2018], 2014.10.30.

[3] J. Considine, "Emergency assessment of oxygenation", Radiometry Medical ApS, Bronshoj, Denmark, 2007.

[4] M. Amini, "A novel optical probe for detection of hypoxia in the deeper layers of human buccal tissue", IEEE Sensors Journal, 2012. 12(6), pp. 9-14, 2016, https://doi.org/10.1109/JSEN.2011.2177082.

[5] D. Epstein and R. Henning, "Oxygen transport variables in the identification and treatment of tissue hypoxia", Heart & Lung, pp. 328-45, July-August, 1993.

[6] A. Fokan and I. Khalil, "Probabilistic estimation of abnormal clinical events using vital sigh correlations for reliable home-based monitoring", Pervasive and Mobile Computing, 38(2), pp. 296-311, July 2017, https://doi.org/10.1016/j.pmcj.2016.12.009.

[7] Cohen, J, "Statistical power analysis for the behavioral sciences" (2nd ed.). Hillsdale, NJ: Lawrence Erlbaum Associates, 1988.

[8] L. Rabiner and B. Juang. "An introduction to hidden Markov models". *IEEE ASSP Magazine*, 3(1), pp. 4-16, 1986.

A Fractional Order Impedance Sensor for Measuring the Quality of Drinking Water

Tarikul Islam, Shibli Shakil, Babita Lohani
Department of Electrical Engineering, Jamia Mllia Islamia
University, Jauhar Ali Marg, Jamia Nagar
New Delhi-110025, India
e-mail: tislam@jmi.ac.in,
shibli.shakil19@gmail.com, babata.lohani@gmail.com

Subash Chandra Mukhopadhyay
Department of Mechanical/Electronics Engineering
Macquire University, New South Wales
Sydney, Australia
e-mail: subhas.mukhopadhyay@mq.edu.au

***Abstract*—A new stick type sensor is fabricated to analyze the quality of drinking water. The sensor has fractional order impedance, which shows constant phase behavior over a wide frequency range (200 kHz to 1 MHz) in drinking water. The parameters of the sensor, such as the constant phase angle (θ) and the fractional exponent ($\alpha \leq 1$) vary with the change in the ionic impurities of water. Fabrication of the sensor is easy, requires cheap materials, and is bulk producible at low cost. For 600 ppm change in the total dissolved solids value of the water sample, there is nearly an 18° shift in the phase angle of the fabricated sensor. The sensor can be utilized to make a prototype probe. A preliminary experimental work is carried out to explore the effectiveness of the sensor to measure the quality of drinking water.**

Keywords- Sensors; fractional order; impedance; drinking water; quality monitoring.

I. INTRODUCTION

Water is mankind’s most precious resource and one of the necessities for the existence of all living beings. Unfortunately, it is often contaminated with various impurities, such as organic, inorganic solvents and microorganisms [1][2]. Disposal of industrial, pharmaceutical and other waste materials to different water resources causes water contamination [2][5]. The most common drug contaminant found in the fresh water is the non-steroidal anti-inflammatory drug ibuprofen. Similarly, the teratogenic and the carcinogenic effects of the phthalate esters, which are used to manufacture different plastic food packages and the other plastic containers pose great danger to all living beings and to the environment [5]. Other common sources of water contamination are the use of nitrate and phosphate salts for agriculture [6][7]. In many developing countries, the contaminated drinking water is a major concern for the human health. Due to inadequate supply of the pure drinking water, people sometimes are compelled to consume untreated ground water or to purchase costly commercially available packaged (plastic container) mineral water [2][5]. Because of high price, sometimes, local vendors add untreated low-cost water to costly mineral water for earning more money. Water impurities can be defined based on the dissolved solids and microorganisms present in the water. A high amount of the dissolved solids can indicate poor water quality, which is harmful for health.

The conventional methods of impurities measurement require separation of the impurities using liquid or gas chromatography technique and subsequently, the mass measurement using a mass spectrometer. The recent technique called electronic tongue is reported for water quality analysis by the authors [8]. The arrays of the sensors in electronic tongue may be of different types, such as surface acoustic wave, conductive polymers, metal oxides, Chem FET, optical, electrochemical, etc. These methods are accurate and reliable but are costly, require skilled man power for their operation, have long analysis time and are not portable for the field testing. Due to the constraints associated with these techniques, the routine analysis of the water samples is normally avoided.

Important parameters for water quality monitoring are pH value, chlorine concentration, flowrate, temperature, turbidity, conductivity etc. A review article on current technologies and future needs of water quality analysis is reported in [9]. Some other reported techniques employ multi sensors fusion data analysis using Dempster -Shafer evidence theory [10] or optical method for bacterial growth monitoring [11]. Some simple methods are present to measure the Total Dissolved Solids (TDS) like the gravimetric method, and the electrical conductivity method [1]. TDS meter is based on the second method, where one can measure the TDS value by dipping the probe into the water sample. Sometimes, a capacitive sensor is used to determine the electrical parameters of water [12] but the sensor has complex design and requires necessary precautions to measure the small capacitance value in presence of unwanted parasitic earth capacitance. According to the world health organization (WHO), the TDS value of the drinking water below 600 ppm is safe for consumption. Therefore, there is a need to develop a quick, low cost and user-friendly probe to measure the ionic impurities of the water sample [1].

This paper presents a constant phase (CP) fractional order sensor to analyze the quality of commercial mineral water available in the market. A fractional order device is identified by two important parameters, (i) the fractional order α, and (ii) the constant phase angle over a certain range of excitation signal frequency. There are several real-world phenomena which show fractional order behavior. An infinite ladder network or a domino network shows the constant phase behavior over a certain frequency range at the fractional order value of nearly 0.5 [13]. The constant behavior is also observed by a conductivity sensor as reported in [14] but rarely any constant phase sensor is available in the market. A constant phase element can also be fabricated by making fractal structure on silicon substrate at $\alpha = 0.46\text{-}0.5$ [15].

In this work, we have studied the response of a fractional order (α) impedance sensor fabricated with double sided copper cladded printed circuit board substrate to measure the ionic impurities of mineral water. Due to the change in ionic impurities, the phase angle and the fractional exponent of the sensor will change. The order and the phase angle vary within 0-1 and 0-90° respectively. Thus, motivation behind this work is to develop a fractional order probe to measure the quality of commercial packaged drinking water. The proposed sensor is easy to fabricate, requires cheap materials for fabrication and is bulk producible at low cost. A preliminary experimental result with some commercial packaged mineral water samples are reported. Theory of the sensor is discussed in section II. In section III, detailed experiments including the sensor fabrication, experimental methods and results are given. Discussion about the experimental results is given in section IV. In section V, the conclusion about the research work is discussed.

II. THEORETICAL ASPECTS

The impedance of a fractional sensor in Laplace form can be expressed by the expression [13], $Z(S) = QS^{-\alpha} = Q\left(j\omega\right)^{-\alpha} = \dfrac{Q}{\omega^{\alpha}}\angle\left(-\dfrac{\pi}{2}\alpha\right)$ where, S (= jω) is the Laplace operator, ω is given by $\left(2\pi f\right)$, with f is the signal frequency, and α is the order of the element. The magnitude (= Q/ω^{α}) depends on the frequency, and the fractional exponent α. But the phase angle $\theta = \left(-\dfrac{\pi}{2}\alpha\right)$ depends on the value of the fractional exponent only.

Thus, a fractional order sensor is identified by the value of fractional exponent and the constant phase angle over a certain frequency range. The value of the fractional exponent varies from -1 to +1. An ideal capacitor, an ideal resistor and an ideal inductor behave as the constant phase device for $\alpha = 1$, $\alpha = 0$, and $\alpha = -1$ respectively. These fractional devices in recent times are found some interesting applications in measurement systems and circuits [14]–[16]. For sensing applications, the characteristics of the constant phase impedance (CPI) in presence of the ionic impurities are mainly functions of three parameters as given by [16] $\theta = f\left(A, t, \sigma\right)$, where, σ represents the ionic concentration of the medium under test, A is the area of contact of the probe with the test medium and t is the thickness of insulation film on the electrodes. However, the porous rough surface of the insulating film plays an important role for the CP behaviour. The measurement of the response is based on the change in phase angle and the fractional order of the CPI due to the change in ionic property of water. Due to the variation of ionic impurities, the parameters of the CPI will change, which in turn helps us to analyze the quality of water.

III. EXPERIMENTS

A. Preparation of the Polymer Insulation Solution

Insulating layer for the fabrication of the CPI is the film of polymethayl metha acrylate (PMMA). 5 % PMMA solution was prepared using PMMA flex and chloroform [16]. Nearly, 5 gm PMMA flex was added in 95 ml chloroform, and then, the solution was stirred on a magnetic hot plate stirrer at 50°C temperature for 2 hrs. Finally, the solution was de-aired to remove the bubbles formed during the stirring process.

B. Fabrication of the CPI Sensor with Double side Copper Cladded PCB Substrate

Fabrication of the sensor requires double or single sided metal coated (copper cladded) printed circuit boards (PCB). These boards are normally used to solder the discrete components of a circuit. The circuit board may be of the copper cladded epoxy resin glass or the copper cladded polyimide substrate, on which a thin porous insulating film was deposited. The porous insulating film may be made of polymer or metal oxide material. While selecting an insulating film, care must be taken to ensure the stability of the insulating film. Desirable characteristics of the fabricated sensor depend on (1) electrode geometries (2) crack free film (3) thickness of the film (4) film uniformity and the morphology of the porous film. Copper cladded polyimide (Upilex, Japan) was used for the CPI fabrication. Polyimide materials are lightweight, flexible, resistant to heat and chemicals and the cost is cheap for the bulk production. A polyimide substrate with double side copper cladded film of size 4 cm × 1 cm was cleaned in dilute sulphuric acid solution (H_2SO_4) for 5 min. The substrate was then dipped into the PMMA solution vertically with the dip in length 20 cm for nearly 30 s.

Figure 1. PMMA coated CPI sensor on polyimide PCB substrate.

An automatic dip coater was used to deposit the PMMA film of nearly 250 µm thickness on both sides of the substrate. The substrate was then dried in air at normal atmospheric condition for 24 hrs. Two copper wires were soldered at the electrodes for the electrical connection. Fig. 1 shows the photo of the PMMA based double sided CPI sensor.

B. *Fabrication of the IDT Electrode CPI Sensor*

For the fabrication of the IDT electrode CPI, the schematic diagram of the sensor is shown in Fig. 2(a). The IDT structure with the dimension shown in the diagram was designed using Autocad software. A screen of the design was prepared. The design was then printed manually on the single side copper cladded polyimide substrate. The substrate with the IDT electrode structure was dipped into the copper etching solution (Ferric chloride) for nearly ~ 10 min to remove the copper layer from the unmasked area. The substrate was then cleaned in DI water and in acetone. Finally, the substrate with the IDT electrode was dipped into the PMMA solution for nearly 30s to deposit the insulating thin film of the PMMA. Fig. 2(b) shows the photo of the IDT sensor. Three IDT structured CPI sensors with different insulation thickness were fabricated to optimize the performances of the sensors. The insulating film deposited on the electrode is having large number of voids of ~ um dimension resulting high effective surface area [16][17]. The FESEM image of the insulating film is shown in Fig. 3. The IDT sensor with single PMMA coating provided better performance and was tested for analyzing the quality of water.

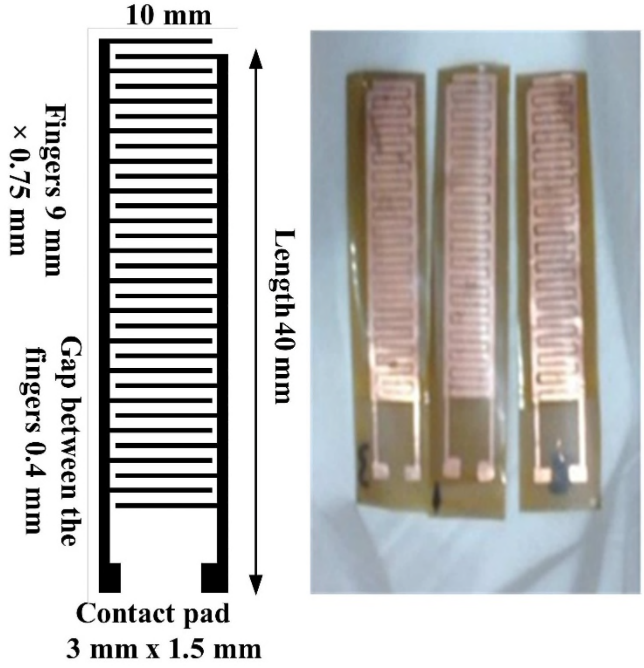

(a) (b)

Figure 2. IDT electrode PMMA coated CPI sensor (a) schematic diagram, (b) photo of the sensors.

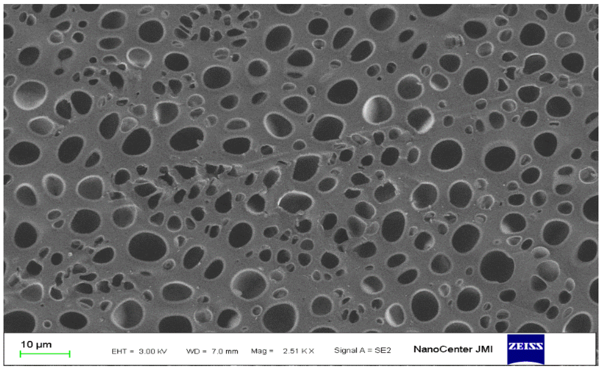

Figure 3. FESEM image of the PMMA insulating film deposited on the electrode.

C. *Testing of the Sensors with Different Water Samples*

Impedance analyzer (LCR meter) was used for testing the fabricated sensors. Parameters like impedance, and phase angle of the sensor in Z-θ mode were measured by the instrument. Each sensor was excited by the sinusoidal AC voltage signal of 1 V (rms) and the frequency was varied in the range of 5 kHz to 5 MHz. For determining the parameters of the CPI, mineral water samples from local market around the University campus, (New Delhi, India) were collected. Initially, the TDS value of each water sample was measured by the commercial TDS meter (accuracy ± 5%). We used the commercially available TDS meter as a reference meter to measure ionic impurities present in the water samples. TDS meter works on conductivity measurement principle. With increase in ionic impurities, the conductivity increases, hence, the TDS value of the water sample increases.

The TDS value of the water samples is shown in Table I. All the water samples are having TDS values, which are within the limit suggested by WHO. Deionized water (DI) which was almost ions free prepared using Millipore water purifying system was also used for testing the sensors (TDS = 0 ppm). Each water sample of 80 ml was taken in a cleaned glass beaker of 100 ml. The sensor was dipped into the beaker at a dip in length of 1 cm. Since, the behavior of the CPI depends on three parameters, so one parameter is the variable that is the ionic concentration of the medium and the other two parameters such as the contact area with the medium and the thickness of insulating film were kept constant. Temperature of the water samples was maintained at 25°C. The readings of the LCR meter in Z-θ mode were acquired into the computer. Each experiment for a water sample of fixed volume was repeated at least for five times to ensure the repeatability of the reading. Average values of five readings were plotted. The maximum standard deviation of the readings of the phase angle value was approximately 0.48. Small deviation from the average value was due to minor variation of the dip in length of the sensor, since the phase angle of the sensor also depends on the contact area. Fig. 4 shows the variation of the phase angle of the sensor. For a certain frequency range, the sensor shows the constant phase behavior. The phase angle of the sensor for different water samples varies with the variation of the signal frequency, but it is almost constant phase over a wide frequency above 200 kHz. There is nearly a 10° shift in the phase angle of the sample 5 from the sample 1, a commercial popular brand (Bisleri). Bisleri is one of the most popular mineral water brands in Delhi. We also performed experiments to determine the response of the sensor with the mineral water sample 1 adulterated by adding impure water having more TDS value. Bisleri was assumed to be a pure reference water and untreated ground water having high TDS value was taken as the impure water.

TABLE I: TDS VALUE OF DIFFERENT WATER SAMPLES

Water Samples	TDS value (ppm)
DI Water	0
Sample 1 (commercial bisleri)	120
Sample 2	250
Sample 3	295
Sample 4	340
Sample 5	600

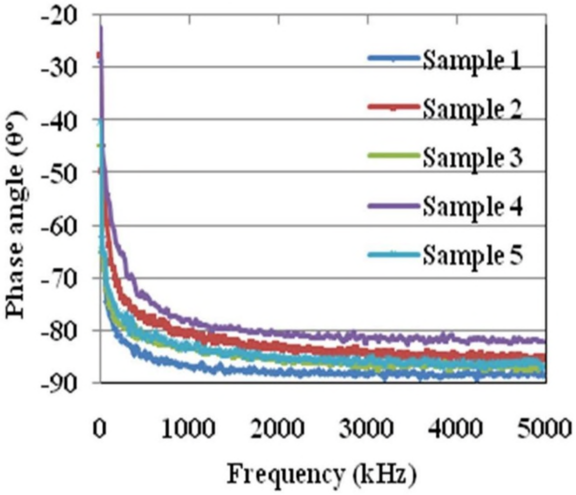

Figure 4. Change in phase angle of the sensor with frequency of different water samples.

The change in phase angle of the sensor for different adulterated water samples with the variation of the frequency is shown in Fig. 5. Again, the CPI sensor shows well defined constant phase behavior above 200 kHz for the adulterated and the pure water but the shift in phase angle of the adulterated sample is very significant. For 20% adulteration of the Bisleri water, there is nearly 20° shift in the phase angle (at f = 400 kHz).

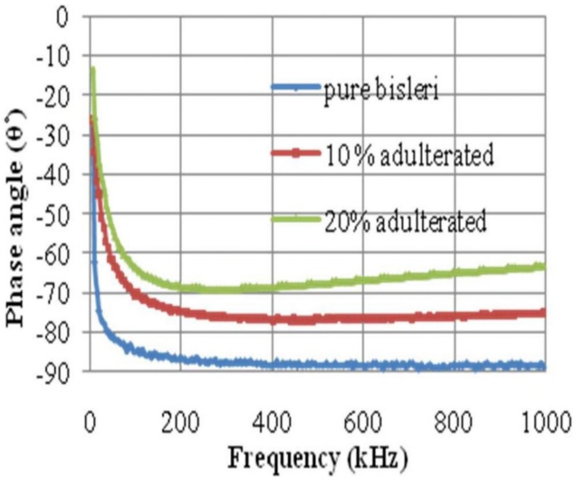

Figure 5. Change in phase angle of the sensor with frequency for the adulterated water samples.

Experiments were then performed with the IDT CPI sensor. Variation of the phase angle with the variation of the signal frequency in the range of 5 kHz-1 MHz is shown in Fig. 6. The IDT sensor also shows the constant phase response over a certain frequency range. However, the sensor in Fig. 1 shows much better constant phase behaviour than the IDT sensor shown in Fig. 2.

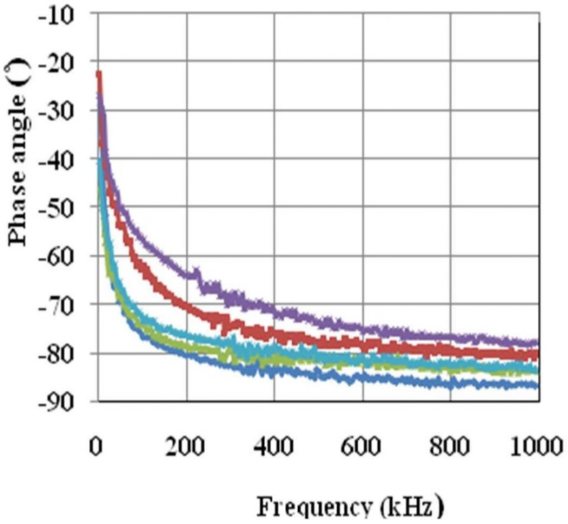

Figure 6. Variation of the phase angle with frequency of the IDT sensor for different pure water samples.

IV. RESULTS AND DISCUSSIONS

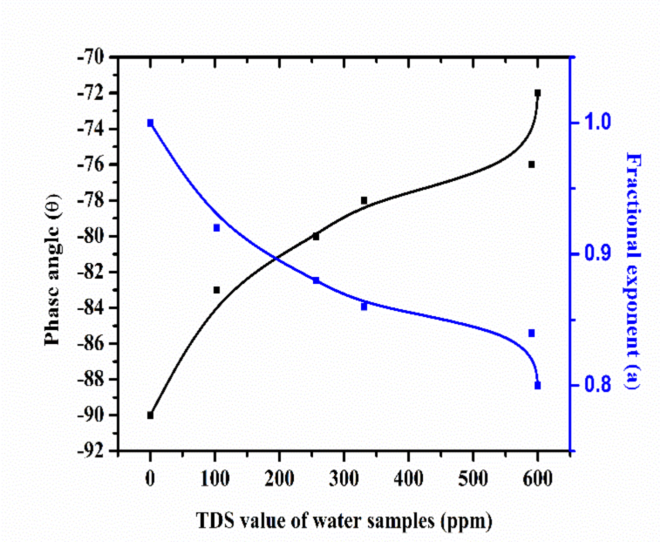

Figure 7. Variation of the phase angle and the fractional exponent with TDS value of the sensor.

The CPI sensor is identified by the constant phase behavior, and the fractional exponent (α), which are independent of the frequency. The parameter α can be determined using the expression $\alpha = -2\theta/\pi$, where θ is the phase angle of the sensor. Using this expression, the values of α were determined at different frequency.

Fig. 7 shows the variation of the phase angle and the fractional exponent of the CPI sensor with the variation of TDS value of the drinking water samples at 400 kHz signal frequency. With increase in TDS value, the conductivity of water increases, hence, the values of the phase angle and the fractional exponent decrease. Therefore, the sensor shows a correlation between the TDS value and the parameters of the CPI sensor.

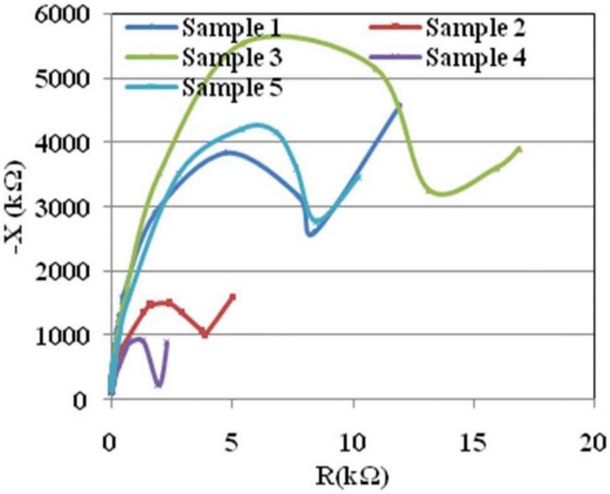

Figure 8. Complex impedance plot of the sensor for different water samples.

Experiments were also performed with DI water (Grade II) having resistivity of 14 MΩ.cm. DI water is almost free from ions, therefore, the sensor is having fractional exponent value close to 1 (α = 1 for perfect capacitor).

The complex impedance data showing the negative of imaginary component of the impedance (Z) is plotted with the real component of the impedance with the variation of the signal frequency. The plot is shown in Fig. 8.

Data of the impedance was obtained from the actual experiments with different water samples in $Z-\theta$ mode of the Impedance analyzer over a frequency range of 5 kHz to 5 MHz. Each of the responses has two distinct parts namely (i) a semicircular part and (ii) a curved straight line. Both the parts vary with the variation of the water types. Semicircular response at higher frequency can be represented by the parallel combination of the resistance and the capacitance. The radius of the semicircle reduces with increase in conductivity of the water samples. The curved straight line towards the lower frequency indicates the diffusion of ions through the macro pores of the insulating film on the electrode [16]. Insulating film of PMMA has macro porous structure as shown in the FESEM image of Fig. 3. Pores are of different size but of the order of micrometer (μm). When the sensor is dip into water, the water molecules contact the electrode through these macro pores. In presence of water, each pore can be represented by an RC network. Values of the equivalent resistance and capacitance of the network depend on the conductivity as well as dielectric constant of the water. Inhomogeneous macrostructure of the insulation and the presence of large number of voids, cause formation of a distributed RC network with different (RC) time constants. Such distribution of the time constant gives the constant phase behavior of the sensor [13], [16]-[17]. For a protype meter, this change in phase shift of the sensor can be converted into a voltage signal using a phase detection electronic circuit.

V. CONCLUSION

This paper presented the initial study of the constant phase sensors and their application for analyzing the quality of drinking water. Fabrication of the sensors is very easy and is bulk producible at low cost. The sensors were tested with pure and the adulterated mineral water samples. The sensors showed the constant phase behavior over a wide frequency range. But the CP and the fractional exponent varied with the variation of the ionic impurities. The phase angle at a particular excitation frequency can be converted into a voltage signal using an interface circuit. The output of the interface can be calibrated to make a stick type probe for the vendors and household application. Initial results showed that the sensor may be suitable to make a ball pen type probe for testing drinking water including its adulteration with impure water. However, detailed investigation with large number of water samples from different commercial brands and different CPI sensors with different pore morphology with more stable insulating films are needed to establish the effectiveness of the sensors for water quality monitoring.

ACKNOWLEDGMENT

This work was supported by Defense Research Development Organization, (DRDO) (Grant no. CC/TM/ERIPR/GIA/16-17/0382/041, New Delhi, India.

REFERENCES

[1] J. Bartram, and R. Ballance, “Water quality monitoring: a practical guide to the design and implementation of freshwater quality studies and monitoring programmes”, CRC Press, 1996.

[2] SC Mukhopadhyay, and A Mason, “Real time water quality monitoring”, SSMI 4, Springer-Verlag Berlin Heidelberg 2013, pp. 1-24.

[3] V. J. Nagaraj, M. Jacobs, K. M. Vattipalli, V. P. Annam, and S. Prasad, “Nanochannel-based electrochemical sensor for the detection of pharmaceutical contaminants in water,” Environ. Science: Processes & Impacts, vol. 16, no. 1, 2014, pp. 135–140.

[4] M. Santono et al., “Investigating single sensor ability in the characterization of drinkable water: a pilot study”, J. Water and Environment, 2016, pp. 1-8.

[5] A. I. Zia, M. S. A. Rahman, and S. C. Mukhopadhyay, “Technique for rapid detection of phthalates in water and beverages,” J. of Food Engineering, vol. 116, no. 2, 2013, pp. 515–523.

[6] X. Wang, et al., “Mechanism and experiment of planar electrode sensors in water pollutant measurement”, IEEE Trans. Inst. and Meas., vol. 64, no. 2, 2015, pp. 516-523.

[7] J. Jiang, X. Wang, R. Chao, Y. Ren, C. Hu, Z. Xu, et al., “Smart- phone based portable bacteria pre-concentrating microfluidic sensor and impedance sensing system,” Sensors and Actuators B: Chemical, vol. 193, 2014, pp. 653–659.

[8] E. Garcia-Breijo, J. Atkinson, and L. Gil-Sanch, “A comparison study of pattern recognition algorithms implemented on a microcontroller for use in an electronic tongue for monitoring drinking waters”, Sensors and Actuators A 172, 2011, pp. 570–582.

[9] Storey MV, B. van der Gaag, and B. P Burns, “Advances in on-line drinking water quality monitoring and early warning system”, Water Research, 45(2), Sep 2011, pp. 741-748.

[10] D. Hou, H. He, P. Huang, G. Zhang, and H. Loaiciga, “Detection of water-quality contamination events based on multi-sensor fusion using an extended Dempster–Shafer method”, Meas. Sci. Technol., 24, 2013, pp. 055801-19.

[11] Bo Højris, and S. C. Boesgaard Christensen, “A novel, optical, on-line bacteria sensor for monitoring drinking water quality”, Scientific Reports, 6, 2016, pp. 23935-45.

[12] H. Golnabi, and M. Sharifian, “Investigation of water electrical parameters as a function of measurement frequency using cylindrical capacitive sensors,” Measurement, vol. 46, no. 1, 2013, pp. 305–314.

[13] S. Roy, “On the realization of a constant-argument immittance or fractional operator”, IEEE Trans. on Circuit Theory, vol. 14, no. 3, 1967, pp. 264–274.

[14] J. Lario-García, and R. Pallas-Areny, “Constant-phase element identification in conductivity sensors using a single square wave,” Sensors and Actuators A: Physical, vol. 132, no. 1, 2006, pp. 122–128.

[15] T. C. Haba, G. L. Loum, and G. Ablart, “An analytical expression for the input impedance of a fractal tree obtained by a microelectronical process and experimental measurements of its non-integral dimension,” Chaos, Solitons & Fractals, vol. 33, no. 2, 2007, pp. 364–373.

[16] T. Islam, Z. U. Rahman, and S. C. Mukhopadhyay, “A novel sol–gel thin-film constant phase sensor for high humidity measurement in the range of 50%–100% RH,” IEEE Sensors, vol. 15, no. 4, 2015, pp.2370–2376.

[17] S. Amand et al., “Constant-phase-element behavior caused by inhomogeneous water uptake in anti-corrosion coatings,” Electrochimica Acta, vol. 87, 2013, pp. 693–700.

Design and Simulation of Low Cost and Low Magnetic Field MRI System

Sweta Ghosh, Vikram Thakur, Rahul Shrestha,
Shubhajit Roy Chowdhury
Biomedical Systems Laboratory, MANAS Group
School of Computing and Electrical Engineering,
Indian Institute of Technology Mandi,
Mandi, India
Emails: sweta_karmakar@students.iitmandi.ac.in,
vikram.th07@gmail.com,
rahul_shrestha@iitmandi.ac.in, src@iitmandi.ac.in

Vinayak Hande
Department of Electrical Engineering,
Indian Institute of Technology Ropar,
Rupnagar, India
Email: vinayak.hande@iitrpr.ac.in

***Abstract*— We present the design of a Magnetic Resonance Imaging (MRI) system based on Helmholtz coil in place of a permanent magnet which is common in commercial MRI systems. Inspired by the homogeneity of the magnetic field of the Helmholtz coil, the design has been proposed. This coil generates a main magnetic field of 0.2T which is a low magnetic field and hence it was possible to make the system low weight to some extent. This makes the proposed design suitable to be taken and operated at remote locations. Along with the main magnetic field, other components are also necessary like the gradient coils, radio-frequency coils and a constant DC current source, to mention a few. The gradient has strength of 75µT/m. The resonating frequency at which the radio-frequency operates is 8.256MHz for 0.2T and the DC source gives a current of 10A with 50V DC which is essential requirement for the operating of the coils. All the components taken together make the whole system.**

Keywords - Helmholtz coil; Maxwell coil; RF coil; constant DC source; homogeneity; magnetic field.

I. INTRODUCTION

Magnetic Resonance Imaging (MRI) is a medical imaging method used in radiology to form images of the biological processes of body in both health and disease conditions. MRI, also known as nuclear magnetic resonance imaging, is a technique for creating images of external as well as internal organs of human body. MRI scanners enable fast, non-invasive, and high-resolution imaging of organs and soft tissue.

MRI was established as a promising diagnostic tool in the beginning of 1980s. While high magnetic field (≥ 1.0T) MRI scanners continue to be the most commonly used, there is growing interest in the utilization of low-field (≤ 0.5T) extremity scanners [6]. They are smaller, less expensive, and easier to install, and allow for quicker patient diagnoses in an office setting. In contrast, high magnetic field scanners have superior image quality because of higher signal-to-noise ratio (SNR), contrast, and resolution [1]. It is possible for low-field scanners to improve image quality by increasing scan duration, although doing so also increases the chance of motion artifacts [1]–[4] While lowfield MRI images may not be able to compete with the quality of those produced using high-field scanners, it is important to consider whether or not they can provide comparable diagnostic capabilities to justify their logistical benefits. When compared with surgical findings, the use of low-field extremity MRI scanners for identifying medical meniscus pathology has been promising (sensitivity, 77%-96%; specificity, 71%-100%); however, the results for identifying pathology of the lateral meniscus have been more variable [5]–[13]. Most of these studies show low-field MRI to be a moderately good identifier of sub-peripheral and meniscus pathology (sensitivity, 75%- 93%; specificity, 94%-100%).

Ghazinoor et al. concluded that their subjective experience is in concordance with many studies demonstrating the high diagnostic value in the use of low-field scanners in musculoskeletal pathology [1]. Tavernier et al. stated that the primary limitation of low-field MRI is lower SNR, which has to be compensated for by increasing the slice thickness, reducing the in-plane resolution, increasing the number of acquisitions (and consecutively the acquisition time), and decreasing the bandwidth [14].

Tavernier et al. concluded that implementation of low-field MRI systems may be useful, especially in orthopaedic centers, or if installation of an additional high-field scanner is not possible because of economic considerations [14]. Blanco et al showed that there is trade-off in image quality towards less resolution due to open structure of these systems [15]. The image quality of low-field scanners is, however, sufficient for interventional use. In a review article, Hayashi et al. noted that no reliable efficacy studies, however, exist comparing the diagnostic capabilities of low- versus high-field scanners [16]. In order to compensate for lower SNR, scanners with low field strength tend to have longer acquisition times, often resulting in greater image degradation due to patient movement.

The current research focuses on the development of a low cost and low magnetic MRI machine for the point of ease testing support. In order to provide the diagnostics support at the point of care, the MRI is proposed to sufficient small weight, because of which Helmholtz coil instead of permanent magnetic is proposed to be used to generate the main magnetic field. The gradient coil is implemented with Maxwell coil. The RF coil design has been implemented based on the papers of Mehmet Bilgen in 2004 and 2001[21-22]. Their study showed implantable coils can work fine having good SNR.

The paper is divided in the following sections. Section II focuses on the design of material and method, Section III discusses the design of the different coils (Helmholtz coil, Maxwell coil; RF coil which has done using concept of COMSOL Multiphysics 5:2 and CST), Section IV discusses results, and Section V the discussion. Section VI concludes the paper.

II. MATERIALS AND METHODS

The MRI in the proposed design is based on Helmholtz Coil. Hence, the main magnetic field is generated using the above mentioned coil. The main magnetic field is of 0.2 T. For such a low magnetic field, the gradient strength is kept at 75µT/m. The gradient fields are necessary to obtain the spatial information about the subject. Maxwell Coil and Saddle Coil were designed as the gradient coils. All these coils are concentric. The inner radius of the system is 40cm, which is enough for head or limbs to be inserted. The inner radius is the radius for the radio-frequency (RF) coil which is a surface coil for the time being.

All the coils are built with annealed copper. For the coils, copper wires were used with AWG gauge size of 11 (2.303mm diameter). Since RF coil is a surface coil it's designed on PCB (Printed Circuit Board) using annealed copper.

III. DESIGN OF COILS

A. *Design of Helmholtz Coil*

Helmholtz coil is basically a pair of coils that are separated from each other at a distance equal to the radius of the coil. The magnetic field is calculated applying Biot Savart's law for Helmholtz Coil. According to Biot Savart's Law,

$$B_1(x)=\frac{\mu_0 n I R^2}{\left(R^2+x^2\right)^{\frac{3}{2}}} \tag{1}$$

where μ_0 is the permeability constant = 4π x 10^{-7} Tm/A. *I* is the current in the coil. *R* is the radius of the coil and *x* is the distance of a point from the coil on the axis of the coil and *n* is the number of turns of the coil. $B_1(x)$ is the magnetic field generated along the axis of the coil due to current *I*.

In case of Helmholtz coil the Biot Savart's Law gets modified a little. In a Helmholtz Coil, a point that is halfway between the coils has a value of *x* equal to *R/2*. The magnetic field at that point due to the two coils is given by,

$$B_1\left(\frac{R}{2}\right)=\left(\frac{8}{5\sqrt{5}}\right)\frac{\mu_0 n I}{R} \tag{2}$$

Since the main magnetic field was 0.2T and the radius was taken to be 30 cm or 0.3 m, so for a current of 10A the number of turns for each coil was obtained as 6675. The orientation of the coil is shown in Figure 1.

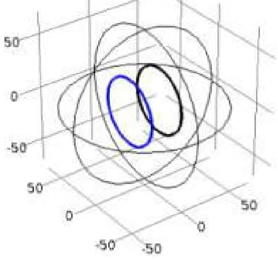

Figure 1. Helmholtz Coil pair of radius 30cm

It is necessary that the main magnetic field be uniform over the volume of interest. Hence, homogeneity becomes one of the important aspects for the main magnetic field or Helmholtz Coil. Homogeneity is calculated from the center of the coil to any particular point and it is measured in percentage change of magnetic field strength from center to any particular point.

$$H(\%)=\frac{\left(B_i-B_0\right)}{B_0}\times 100\% \tag{3}$$

H is the homogeneity or percentage change of magnetic field strength at any point from the center. B_i is the magnetic field at any point in the volume and B_0 is the magnetic field at the center. Generally volumes of spheres or cylinders are considered to specify homogeneity. Here a sphere has been chosen to calculate homogeneity in the Helmholtz coil. From the homogeneity, the region of study can be predicted very well, thus defining the area where to place the patient.

B. *Design of Gradient Coils*

Gradient coils provide some deliberate inhomogeneities which can be used to frequency encode spatial information of the signal returned by the sample or subject. Maxwell coil and Saddle coil has been used as the gradient coils. While Maxwell coil provide the gradient field along the *z* axis (longitudinal gradient), Saddle coils provide the gradient strength along the *x* and *y* axis (transverse gradients) respectively. The basic equation governing the linearly varying the gradient magnetic field is given by,

$$\begin{aligned} B_Z(x,y,z) &= B_0+\frac{\partial B_Z}{\partial x}x+\frac{\partial B_Z}{\partial y}y+\frac{\partial B_Z}{\partial z}z \\ &= B_0+G_x x+G_y y+G_z z \end{aligned} \tag{4}$$

where B_0 is the main magnetic field. G_x and G_y are the transverse gradient and G_z is the longitudinal gradient. Maxwell coil is governed by the equation,

$$B_Z=\frac{\mu_0 I a^2}{2\left[\left(\frac{d}{2}-z\right)^2+a^2\right]^{\frac{3}{2}}}-\frac{\mu_0 I a^2}{2\left[\left(\frac{d}{2}+z\right)^2+a^2\right]^{\frac{3}{2}}} \tag{5}$$

Here, B_z is the magnetic field along the *z* axis due to the current in the coils. μ_0 is the permeability constant, *I* is the current in coil (in Amperes), *a* is the radius of coil (in meters) and *z* and *d* are the distance of a point from the coil on the axis (in meters) and the distance between the coils respectively. A gradient strength of 75µT/m has been considered having a current of 5A in a coil of radius 25 cm. The orientation of Maxwell coil is shown in Figure 2.

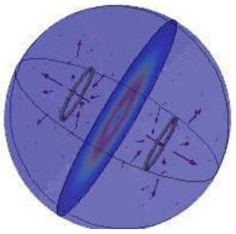

Figure 2. Maxwell coil orientation and magnetic lines of force

The transverse gradient i.e. gradients in the *x* and *y* directions is obtained from the basic equation,

$$B_Y(y,z) = \frac{\mu_0 I}{2\pi}\left[\frac{b-y}{(b-y)^2+(d-z)^2}\right] \tag{6}$$

B_z represents the gradient field along *y* direction and *b* and *d* are the co-ordinates in the *yz* plane. For *x* direction the Saddle coil is rotated 90degrees.

C. Design of Radio-Frequency Coil

The radio-frequency (RF) radiation on the magnetization of the sample is important to obtain images. The RF coil consists of a transmitter and receiver section. The transmitter section radiates the sample with a RF field in order to tip the magnetization away from equilibrium position and that it can generate a detectable NMR signal. The receiver section receives the signal and transforms the signal from analog to digital using some necessary circuitry.

The protons in the subject or patients go from one energy state to another energy state by releasing energy. That is they emit photon of some frequency to move from an excited state to equilibrium state. This frequency is directly proportional to the magnetic field strength. The relation between the resonating frequency and the main magnetic field is given by,

$$\varpi = \gamma B_0 \tag{7}$$

where ϖ is the angular frequency, B_0 is the main magnetic field and is the gyromagnetic ratio for protons whose value is 42.58 MHz/T. From the fact that main magnetic field is 0.2T the resonating frequency comes out to be 8.526MHz. This frequency is also called the Larmor frequency of the nucleus. For designing the coil, it is required take the length of the coil less than the wavelength. The length of the wire was taken at 1/20th of the wavelength which is 1.76m. The design is simple rectangular spiral coil (surface coil) whose dimension is 20cm by 10cm.

D. Design of Constant DC source

The voltage-mode feedback approach in circuit design is becoming more common; because circuits designed using this approach will always work better at low speed-high accuracy, than its current-mode counterpart. Therefore many systems could take advantage of voltage-mode feedback over a wide field of applications like low frequency voltage or current reference design.

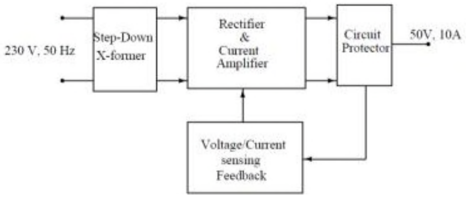

Figure 3. Block diagram of constant DC current source

The block diagram of constant DC current source is shown in Figure 3. Step down transformer converters 230V, 50Hz mains power supply to 50V, 50Hz. Rectifier convert it into DC voltage. Later sensing feedback makes sure that the output voltage and currents are 50V (DC) and 10A (DC), respectively.

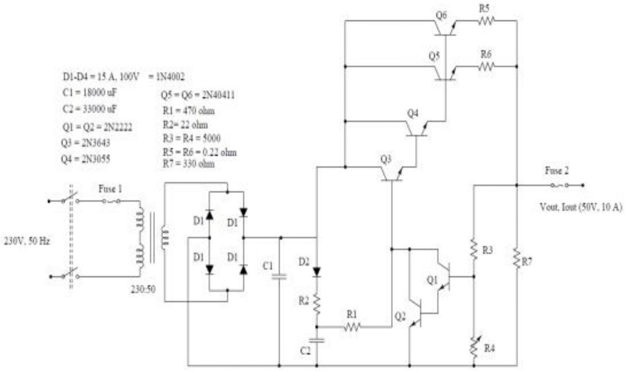

Figure 4. Circuit diagram of constant DC current source

Circuit diagram of constant DC current source is shown in Figure 4. Rectifier contains bridge type rectifier with large value capacitor. Sensing and feedback circuit consist of resistors R3 and R4 along with two Darlington BJT pairs of Q1-Q2 and Q3-Q4. The feedback factor in terms of voltage is given in eq. 8.

$$feedback(V) = I_{B_1}\left(\frac{R_4 R_7}{R_3 + R_4}\right)(\beta_5 + \beta_6)(\beta_1\beta_2\beta_3\beta_4) \tag{8}$$

By selecting larger values of beta's (*β*), the feedback factor can be increased. However, large power rating along with large beta BJTs increases the cost further.

IV. RESULTS

The simulations were performed in COMSOL Multiphysics and CST (Computer Simulation Technology). In both softwares, a 3-Dimensional design is provided, material is also assigned and also the study type is given. The results are discussed in the subsections.

A. Simulation of Helmholtz Coil

The model of Helmholtz Coil has been built in COMSOL Multiphysics. The coil was designed for a magnetic field strength of 0.2T. The inner radius of the coil has been kept 30 cm or 0.3 m while the outer radius extends upto 59 cm. The material of the coil was copper having a gauge size of 11. Using the equation of the magnetic field the number of turns obtained was 6675 for a current of 10A. Having considered these specifications the magnetic flux density was obtained from the simulation. The results are shown in Figure 5 below.

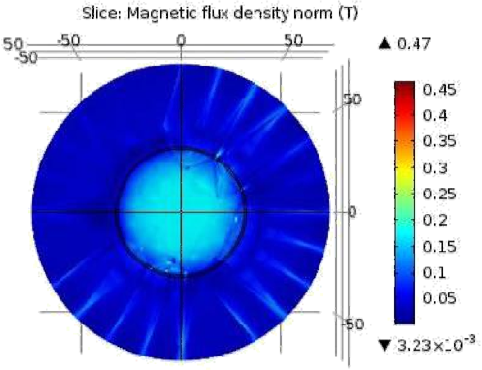

Figure 5. Magnetic flux density at the center of the coil.

Homogeneity of Helmholtz Coil is considered to be uniform i.e. magnetic field is uniform within the coil. The uniformity of the coil can be observed from the figure above. Also, a line graph has been obtained from the simulation as shown in Figure 6.

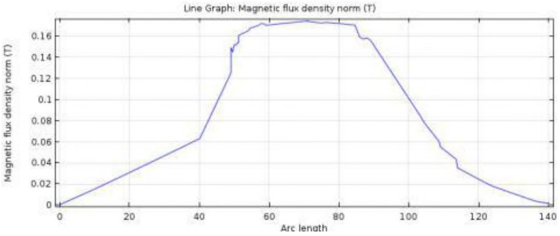

Figure 6. Homogeneity of Helmholtz coil

B. *Simulation of Maxwell Coil*

Maxwell Coil is anti-Helmholtz coil whose governing equation has been given above. Maxwell Coil has been used for longitudinal gradient and Saddle coil has been used for transverse gradient. In Maxwell coil the distance between the coils is √3 times the radius of the coil. The radius of the coil has been taken as 25 cm and the current 5A. Having these specifications the number of turns obtained was 125 and the slope or gradient strength was 75µT/m. The slope was determined from this graph in Figure 7.

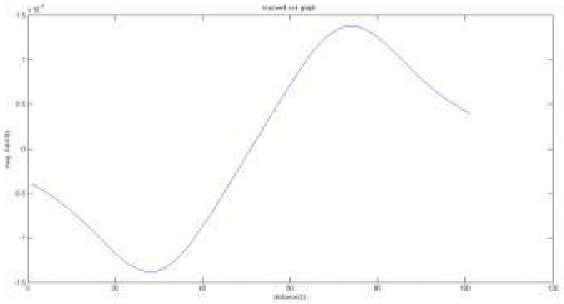

Figure 7. Slope of the Maxwell coil

The simulation result in Figure 8 shows the distribution of magnetic flux density of the Maxwell coil. The magnetic flux varies from the center towards outside.

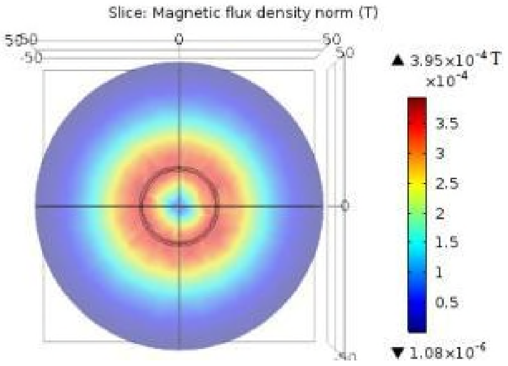

Figure 8. Magnetic flux distribution of Maxwell coil

C. *Simulation of RF coil*

When it comes to radio-frequency coil (RF coil), it is one of the important part of the MRI system. The RF coil is responsible for images developed from a MRI system. The RF coil consists of two parts, the transmitter part and the receiver part. Both these parts are designed separately. A basic design of the transmitter part is given in Figure 9. It simply consists of a rectangular spiral coil which was simulated in Computer Simulation Technology (CST). The model is shown in Figure 9.

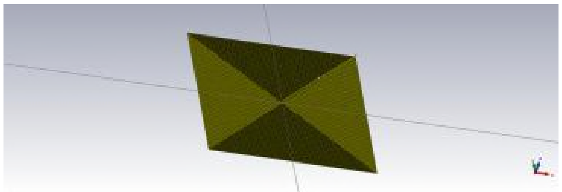

Figure 9. Model of simple transmitter part

The magnetic field and the electric field generated by this model are shown in Figures 10 and 11, respectively.

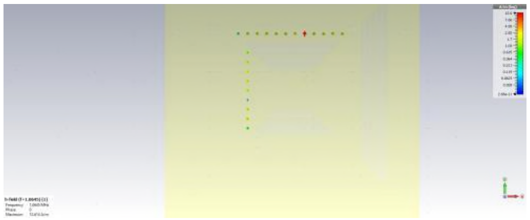

Figure 10. Magnetic field by the transmitter part

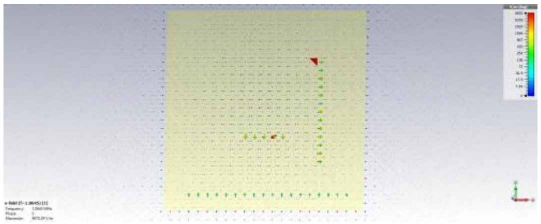

Figure 11. Electric field of the transmitter part

D. Experimental setup of constant DC source

Figure 12. Measurement set-up for constant DC current source

Measurement set-up is shown in Figure 12. Input single phase- secondary's AC is recorded i.e. 45 V. Output DC voltage (50 V : clearly visible) and DC current (10 A : little hazy) are shown here. Due to large value capacitor we get 50V DC after applying 45 V AC as input. The outputs are observed to be constant at 10A with 50V DC. This circuit is useful as voltage and current reference circuit for powering up the low cost MRI systems.

V. DISCUSSION

The various results are obtained from COMSOL Multiphysics5.2 for single slice and multi-slice in multidomain and X-Y plane. The results show the distribution of magnetic field in coil, surface charge density of the coils and percentage of homogeneity of magnetic field at the centre of the two coils. Helmholtz coil and Maxwell coil have these results. The simulation results give insights on placement of the subject inside the MRI machine for MR imaging. Figure 3 shows the inner side edge of second coil, which the reference edge is taken for Helmholtz coil from where we started our studies. However in the RF coil, studies were performed in CST. In that simple design results were obtained for 1V input voltage. And the output for the constant DC current source is observed to be 10A with 50 V DC.

A. Helmholtz coil and Maxwell coil

Simulation studies regarding the Helmholtz coil as well as the Maxwell coil shows the distribution of magnetic flus density of the coils. Regarding the Helmholtz coil the flux density was found to be 0.2T (calculated and simulated). For the Maxwell coil, the flux density is zero at the center of the coil, which is also depicted by the simulation result. From the flux density graph in figure and the homogeneity graph in figure it can clearly be inferred that the field is homogeneous within the coil. The flux density is constant within some region of the coil (region of study) inferring that field is homogenous in that region.

A study of homogeneity along the radial length of the coil is given in TABLE I. And it can be seen that homogeneity lies within ±2% in the region of study.

B. RF coil

The design of RF coil is simple rectangular spiral coil. And it's electric and magnetic field has been shown in Figures 8 and 9. Using these two fields the RF coil can be easily designed. A magnetic field of 1.3T is within the coil and an electric field of 867 V/m is within the coil.

C. Constant DC current source

An input of 45 V at the single phase secondary's AC is recorded while at the output DC voltage 50 V is recorded. A DC current of 10A with 50 V is observed at output.

TABLE I. HOMOGENEITY OBTAINED FROM SIMULATION OF HELMHOLTZ COIL

Radius (cm)	**Homogeneity (%)**
4.29	0.33
11.5	0.48
11.85	0.47
12.9	1.8
14.53	2.63
25.85	39

D. Comparison with existing MRI systems available in literature

The cost and performance of the proposed MRI system has been compared with MRI systems available in literature and presented in TABLE II.

TABLE II. COMPARISON OF PROPOSED MRI WITH MRI AVAILABLE IN LITERATURE

Type of MRI	**Cost/Estimated Cost**	**Homogeneity of magnetic field**	**Weight of the system**
Proposed MRI	INR 10 lacs	1%	2 tons
Esaote® MRI [23]	INR 2.5 crores	0.8%	15 tons

The results shown in TABLE II clearly indicate that except for a marginal loss in homogeneity, there is a tremendous reduction in cost and weight of the MRI system which will prove beneficial for the implementation of a low cost transportable MRI system in a developing country like India.

VI. CONCLUSION

This paper presents a design of Helmholtz coil, Gradient coil, RF coil and constant DC current source for the development of a low cost and low magnetic field MRI system. The simulation results have been obtained for Helmholtz coil and Maxwell coil in z-direction for magnetic flux density, magnetic field at the centre of the coil and over the surface of the coils obtained from COMSOL Multiphysics 5.2. The RF coil was simulated in CST environment to obtain the electric field and the magnetic field which gave a rough idea regarding the design of RF coil. The plots obtained from the COMSOL and our calculated data shows the exact same values prove that our approach is accurate. Our study reveals that there occurs homogeneity in Helmholtz coil where we can place subject for study. We have calculated and validated through simulation that homogeneity at the centre of Helmholtz coil is about ±2 per cent over the region of study. The constant DC source gave an output of 10A with 50 V which is our requirement. This machine will be useful and harmless for mankind and will give the better results as compared to bulky machines.

ACKNOWLEDGMENTS

The authors would like to thankfully acknowledge Indian Institute of Technology Mandi, Indian Institute of Technology Ropar and PGIMER Chandigarh for supporting this study.

REFERENCES

[1] S. Ghazinoor and J. V. Crues, “Low field mri: a review of the literature and our experience in upper extremity imaging,” Clinics in sports medicine, vol. 25, no. 3, pp. 591–606, 2006

[2] S. Ghazinoor, J. V. Crues, and C. Crowley, “Low-field musculoskeletal mri,” Journal of Magnetic Resonance Imaging, vol. 25, no. 2, pp. 234–244, 2007.

[3] R. Loew, K. Kreitner, M. Runkel, J. Zoellner, and M. Thelen, “Mrarthrography of the shoulder: comparison of low-field (0, 2 t) vs highfield (1.5 t) imaging,” European radiology, vol. 10, no. 6, pp. 989–996,2000.

[4] K. Woertler, M. Strothmann, B. Tombach, and P. Reimer, “Detection of articular cartilage lesions: Experimental evaluation of low-and highfield-strength mr imaging at 0.18 and 1.0 t,” Journal of Magnetic Resonance Imaging, vol. 11, no. 6, pp. 678–685, 2000.

[5] M. J. Barnett, “Mr diagnosis of internal derangements of the knee: effect of field strength on efficacy.” AJR. American journal of roentgenology, vol. 161, no. 1, pp. 115–118, 1993.

[6] A. Cotten, E. Delfaut, X. Demondion, F. Lap`egue, M. Boukhelifa, N. Boutry, P. Chastanet, and F. Gougeon, “Mr imaging of the knee at 0.2 and 1.5 t: correlation with surgery,” American Journal of Roentgenology, vol. 174, no. 4, pp. 1093–1097, 2000.

[7] F. Sp, W. Del Pizzo, F. Mj et al., “Accuracy of diagnoses from magnetic resonance imaging of the knee,” Clinical Journal of Sport Medicine, vol. 1, no. 3, p. 212, 1991.

[8] J. L. Glashow, R. Katz, M. Schneider, and W. Scott, “Double-blind assessment of the value of magnetic resonance imaging in the diagnosis of anterior cruciate and meniscal lesions.” J Bone Joint Surg Am, vol. 71, no. 1, pp. 113–119, 1989.

[9] J. Kinnunen, S. Bondestam, A. Kivioja, J. Ahovuo, S.Toivakka, I. Tulikoura, and T. Karjalainen, “Diagnostic performance of low field mri in acute knee injuries,” Magnetic resonance imaging, vol. 12, no. 8, pp. 1155–1160, 1994.

[10] H. S. Lokannavar, X. Yang, and H. Guduru, “Arthroscopic and lowfield mri (0.25 t) evaluation of meniscus and ligaments of painful knee,” Journal of clinical imaging science, vol. 2, 2012.

[11] B. R. Mandelbaum, G. A. Finerman, M. A. Reicher, Hartzman, L. W. Bassett, R. H. Gold, W. Rauschning, and F. Dorey, “Magnetic resonance imaging as a tool for evaluation of traumatic knee injuries anatomical and pathoanatomical correlations,” The American journal of sports medicine, vol. 14, no. 5, pp. 361–370, 1986.

[12] K.-A. Riel, M. Reinisch, B. Kersting-Sommerhoff, N. Hof, and T. Merl, “0.2-tesla magnetic resonance imaging of internal lesions of the knee joint: a prospective arthroscopically controlled clinical study,” Knee Surgery, Sports Traumatology, Arthroscopy, vol. 7, no. 1, pp. 37–41, 1999.

[13] R. T. Blanco, R. Ojala, J. Kariniemi, J. Per¨al¨a, J. Niinim¨aki, and O. Tervonen, “Interventional and intraoperative mri at low field scanner– a review,” European journal of radiology, vol. 56, no. 2, pp. 130 142, 2005.

[14] T. Tavernier and A. Cotten, “High-versus low-field mr imaging,” Radiologic clinics of North America, vol. 43, no. 4, pp. 673–681, 2005.

[15] N. Hayashi, Y. Watanabe, T. Masumoto, H. Mori, S. Aoki, K. Ohtomo, O. Okitsu, and T. Takahashi, “Utilization of low-field mr scanners,” Magnetic resonance in medical sciences, vol. 3, no. 1, pp. 27– 38, 2004.

[16] H. Yoshioka, S. Ito, S. Handa, S. Tomiha, K. Kose, T. Haishi, A. Tsutsumi, and T. Sumida, “Low-field compact magnetic resonance imaging system for the hand and wrist in rheumatoid arthritis,” Journal of Magnetic Resonance Imaging, vol. 23, no. 3, pp. 370–376, 2006.

[17] A. K. Scheel, K. A. Hermann, S. Ohrndorf, C. Werner, C. Schirmer, J. Detert, M. Bollow, B. Hamm, G. A. M¨uller, G. R. Burmester et al., “Prospective 7 year follow up imaging study comparing radiography, ultrasonography, and magnetic resonance imaging in rheumatoid arthritis finger joints,” Annals of the rheumatic diseases, vol. 65, no. 5, pp. 595– 600, 2006.

[18] B. Ejbjerg, E. Narvestad, M. Szkudlarek, J. Jacobsen, “Öptimised low cost low-field dedicated extremity mri can provide similar information on wrist and mcp joint synovitis and bone erosions as expensive conventional high-field mri arthritis-a comparison with conventional’high-field mri,” in Ann Rheum Dis, 2002.

[19] J. V. Crues, F. G. Shellock, S. Dardashti, T. W. James, and O. M. Troum, “Identification of wrist and metacarpophalangeal joint erosions using a portable magnetic resonance imaging system compared to conventional radiographs.” The Journal of rheumatology, vol. 31, no. 4, pp. 676–685, 2004.

[20] H. Lindegaard, J. Vallø, K. Hørslev-Petersen, P. Junker, and M. Østergaard, “Low field dedicated magnetic resonance imaging in untreated rheumatoid arthritis of recent onset,” Annals of the rheumatic diseases, vol. 60, no. 8, pp. 770–776, 2001.

[21] M. Bilgen, “Simple low cost multipurpose RF coil for MR microscopy at 9.4 T”, Magnetic Resonance in Medicine, Vol, 52, pp. 937 – 940, 2004.

[22] M. Bilgen, I. Elshafiey, and P. A. Narayana, “ In vivo magnetic resonance microscopy of rat spinal cord at 7 T using implantable RF coils”, Magnetic Resonance in Medicine, Vol, 46, pp. 1250 – 1253, 2001.

[23] https://www.esaote.com/en-IN/dedicated-mri/mri-systems/p/s-scan/ [accessed August 2018]

Modeling and Simulation of Various kinds of Blockage in Carotid Artery

Kshitij Shakya , Shubhajit Roy Chowdhury
Biomedical Systems Laboratory, MANAS Group
School of Computing and Electrical Engineering, Indian Institute of Technology Mandi,
Mandi, India
Email: d17016@students.iitmandi.ac.in, src@iitmandi.ac.in

Abstract — **This paper focuses on the blood flow in blood vessels and the obstruction faced by it due to plaque which gets accumulated due to deposition of fat and cholesterol on the side walls of the blood vessels. The current research analyses the blood velocity profile and the changes in pressure. The deposition of plaque from initial level to complete blockage of the artery and its consequence on blood flow is also presented in this article. A three dimensional model of a blood vessel along with the deposition of plaque on it has been developed and simulated in Comsol Multiphysics 5.3. This study assumes that the fluid is non-Newtonian, viscous and compressible. Fluid flow is laminar and the arterial wall is elastic. Properties of blood vessel, fat and blood were assigned to the materials of geometry used for simulation. The simulation studies show the hemispherical blockages of carotid artery are really dangerous and may be a cause of concern for imminent ischemic cerebrovascular accident or stroke.**

Keywords- COMSOL Multiphysics; blood vessel; Spherical and hemispherical blockages; carotid arterydisease, computational fluid dynamics.

I. INTRODUCTION

Analysis of flow conditions in the blood vessel is very important to avoid various cardiovascular and cerebrovascular diseases. One of the major arteries, named carotid artery, is often studied for prognosticating imminent cardiovascular and cerebrovascular disorders. The carotid artery disease (CAD) is characterized by the deposition of fat and cholesterol which takes the form of a plaque. It keeps on depositing on the walls of blood vessel until it completely blocks the blood vessel. The severe cases result in heart attacks or even cardiac arrest or cerebral ischemic attack. Early detection of this disease is very important.

Clinical symptoms of carotid artery disease may manifest themselves as stroke or transient ischemic attack [1]. Most cases of carotid artery stenosis are caused by atherosclerotic plaque as part of generalized atherosclerotic disease. Carotid artery stenting (CAS) has been initially used as an alternative treatment option in patients not eligible for surgery [6]. Numerous non-randomized and some randomized studies have assessed the safety and efficacy of CAS in so-called high risk patients. It is hard to reconcile the modest number of patients who are at increased 10-year risk by the Framingham cardio-vascular (CV) risk model with the observation that the lifetime risk of coronary artery disease (CAD) starting at age 40 years is 49% for men and 32% for women [3]. Several studies have shown that plaque presence is associated with systolic blood pressure, use of tobacco, the total to high-density lipoprotein cholesterol ratio, and body-mass index or weight [4]. Carotid plaque is associated with traditional and non-traditional CV risk factors. Several studies have shown that carotid plaque, either alone or combined with other screening tests and information from the patient's history, predicts the presence of cardiac ischemia and angiographic CAD [2].

The current research analyses the various blood flow velocities, lateral minimum and maximum velocity and also the pressure experienced by the arterial wall and the structure of plaque causing obstruction. Our aim is to compare the scenarios between a healthy artery and the artery with disease describing the changes in the blood flow, plaque formation, blood flow velocity and pressure. This computer simulated model is helpful in analysing the possibility of occurrence of CAD and learning the behaviour and consequences of the plaque getting deposited regularly. The model also simulates the formation and growth of the plaque and observes the changes in blood flow which is faster, simpler and safer before doing the treatment.

This paper is organized as follows: Section II focuses on the modeling of the carotid artery, Section III is about results and their discussion and, lastly, Section IV concludes the paper.

II. MODELING OF CAROTID ARTERY

In the current work Comsol Multiphysics® has been used to model the geometry of the artery and do the desired simulations. A cylindrical shaped structure of 6 mm radius and 50 mm length has been taken to model the artery. To design two different types of blockages, a sphere with 3 mm radius was embedded on the upper wall of the artery and, in the second case, two hemispherical chords like structure were embedded on the upper and lower wall of the artery. For simulation of the blood flow inside the artery, it was assumed to have a3D laminar flow. For studying the effect of blood flow on the walls of the carotid artery, solid mechanics accompanied by a stationary study solver have been used. The material for the blood has been assumed to be non-Newtonian, viscous, and compressible and the artery walls have been assumed to be elastic. The blood flow is governed by the continuity equation and Navier-Stokes equation.

The model contains three domains, one forms the cylinder containing the walls of the artery, the second forms the space where blood flows and the third is for the fat or cholesterol structure forming the plaque.

TABLE I. MATERIAL PROPERTIES USED FOR SIMULATION

Properties	**Blood**	**Artery**	**Fat deposit**
Density (Kg/m^3)	1060	1.06e3	1050
Dynamic Viscosity(Pa.s)	0.005	-	-
Young's modulas (MPa)	-	2	20
Poisson's ratio	-	0.49	0.11

The flow under laminar flow physics was modelled for blood as a non-Newtonian fluid with no slip boundary condition. Two boundaries for inlet and outlet flow have been selected with inlet velocity of 0.15m/s and outlet pressure of 0 atm.

Two types of cholesterol deposits are modelled against the artery wall: one is sphere shaped and the other is hemispherical type whose parameters used for simulations are shown in Table I. A 3D shape of a cylindrical blood vessel is shown in Figure 1 with cross section and longitudinal view.

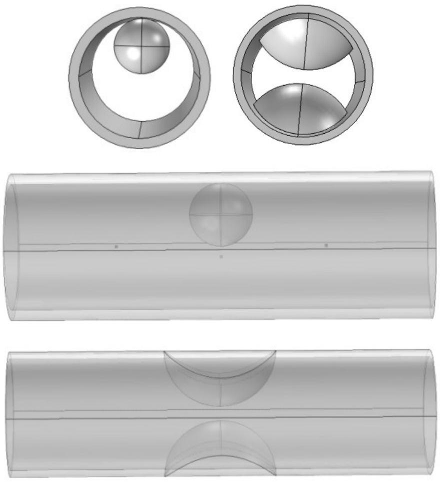

Figure 1. Cross section and longitudinal view of two different types of blockage

The outer cylinder in the above images can be viewed as blood vessel, the spherical and two hemispherical geometries as the fat deposit and the space inside the cylinder as the channel for blood flow. The initial radius or sphere and hemispheres were 3 mm and 5 mm, respectively and this was incremented to increase the range of blockage.

The thickness of the artery has been taken as 1 mm with 8 mm radius and 60 mm length. The inlet blood flow velocity has been taken as 0.15 m/s throughout the simulation. A parametric sweep has been applied to the radius of the sphere and hemisphere to model the variations in fat deposit and hence finding the changes in the blood flow and pressure.

A finite element mesh has been created for the described geometry with free tetrahedral and fluid dynamics physics for the blood flow channel and free tetrahedral and general physics for the remaining geometry with the number of vertex elements being 29, the number of edge elements being 572, the number of boundary elements being 7042 and number of elements being 49038.

III. RESULTS AND DISCUSSION

The artery with no blockage is modeled first and its velocity profile is shown in Figure 2. The artery with the spherical blockage is modeled next and shown in Figure 3. In Figure 3, the initial blockage sphere of 3 mm radius has been shown. Figure 4 depicts spherical blockage of artery of 6 mm radius.

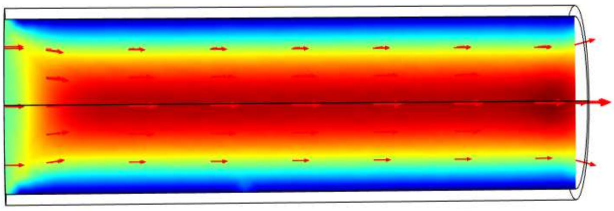

Figure 2. Artery with no blockage

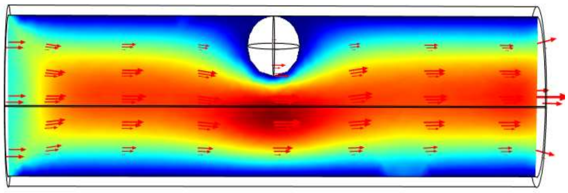

Figure 3. Spherical blockage of 3mm radius

In Figures 2, 3 and 4, the velocity of blood at different points is indicated by the colour code with red having the highest value and blue having the lowest.

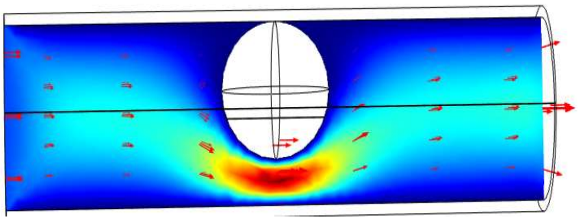

Figure 4. Sphere blockage of 6mm radius

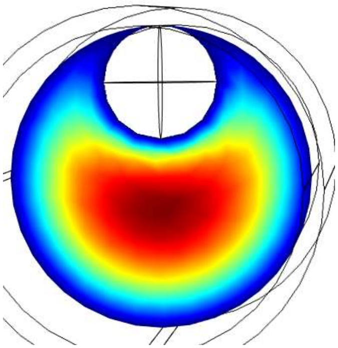

Figure 5.Cross section view of 3mm spherical blockage

The pressure experienced by the blockage in both cases above are shown in Figures 6 and 7 below.

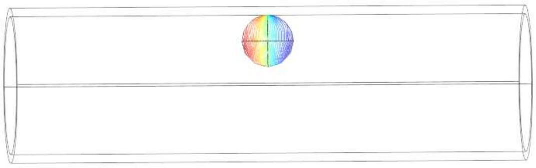

Figure 6. Pressure experienced by blockage due 3mm to blood flow

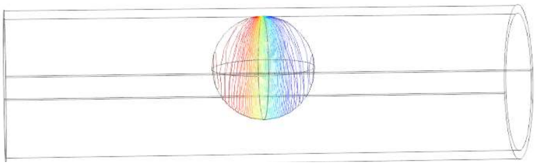

Figure 7. Pressure experienced by the 6mm spherical blockage

Figures 6 and 7 show the pressure distribution on the spherical blockage and the colour pattern shows that the smaller sphere experiences less pressure than the bigger one having 9.35 Pa and 427.5 Pa, respectively.

Next, simulations are repeated for the hemispherical blockage. The radii of the blockages have also been varied to study the velocity profile of the blood. The initial radius has been taken as 5 mm and the final 9 mm. Figure 8 depicts velocity profiles of the carotid artery with hemispherical blockages of radius 5 mm. Figure 9 shows the velocity profile of carotid artery with hemispherical blockages of radius 9mm. Figures 10 and 11 show the blood pressure profiles of carotid artery with hemispherical blockages radius 5 mm and 9 mm, respectively.

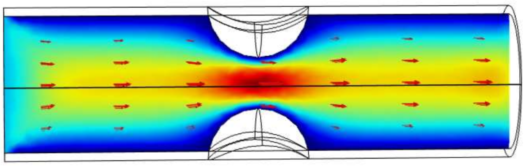

Figure 8.Artery with two hemispherical blockages with big gap

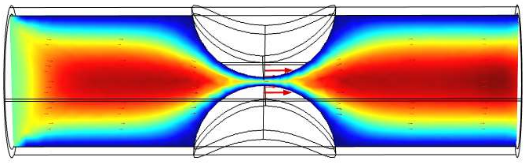

Figure 9. Artery with two hemispherical blockages with narrow gap

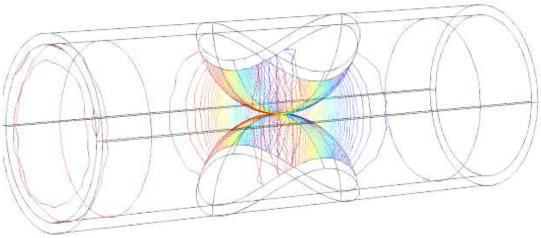

Figure 10.Pressure profiles of hemispherical blockage with narrow gap

In the previous paragraph, we have seen blood flow through the carotid artery under various conditions. Starting from the point where there is no blockage, we see that the velocity is uniform throughout the artery. In the midway, it is highest and at the walls it is lowest. This profile signifies a healthy artery.

Moving to the spherical blockage artery, we see that the velocity just beneath the sphere increases and then decreases. The artery with bigger sphere blockage in Figure 4 can be clearly seen to have decreased its velocity by the density of red color. Looking at the pressure profile of the fat content, it shows the increased pressure in the direction of flow and decreased on the other side.

The comparison between the healthy artery, the spherical blockage artery and two hemispherical blockage artery is done below on the basis of pressure experienced at the side walls and velocity. For this, a point is marked on the side wall of the artery to measure pressure for every increment in the blockage. For measuring velocity, a point at the bottom of the artery has been marked. Figure 13 shows the velocity measured for different radii of the spherical blockage. Table 2 shows the velocity of blood flow against changing different radii of the sphere.

TABLE II. VELOCITY MEASURED FOR SPHERICAL BLOCKAGE

Radius of sphere (mm)	Velocity of blood(m/s)
3	0.182
3.5	0.256
4	0.393
4.5	0.802
5	1.521
5.5	3.868

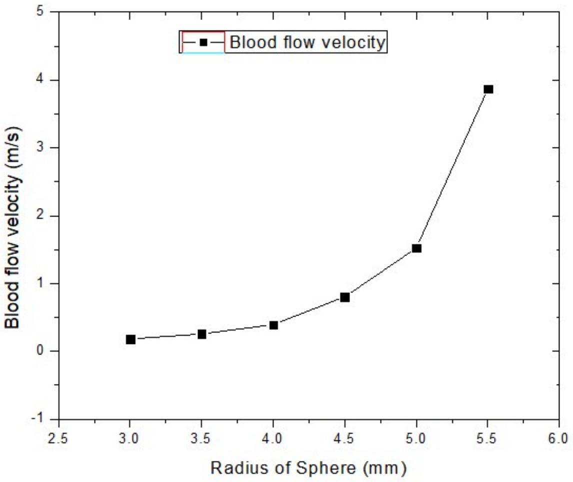

Figure 11.Velocity changes for spherical blockage

Figure 12 depicts the velocity measured at different radii of two hemispherical blockages. Table 3 depicts the velocity of blood flow in the artery for different radii of hemisphere in hemispherical blockage.

TABLE III. VELOCITY MEASUREMENT FOR HEMISPHERICAL BLOCKAGES

Radius of hemisphere(mm)	Velocity of blood(m/s)
4	0.35
5	0.39
6	0.47
7	0.57
8	0.63
9	0

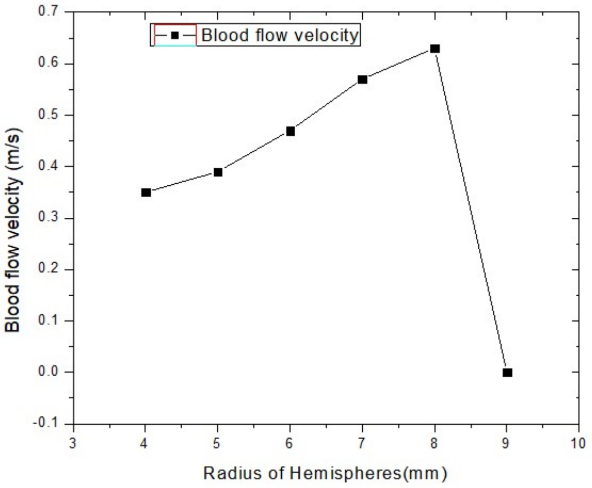

Figure 12.Velocity changes for hemispherical blockage

The graph is plotted next to visualize the above table values and shows one peculiar thing, after raising, this graph suddenly drops to zero. It is due to the fact that here both the hemispheres have touched each other and at that point blood doesn't flow anymore but from the side ways. This sets up a perfect condition for ischemic cerebrovascular accident or stroke. Table 4 shows the pressure experienced by the artery wall due to spherical blockage. Given below is the table for pressure on side walls against radius of sphere (Table 4).

TABLE IV. PRESSURE ON ARTERY WALL DUE TO SPHERICAL BLOCKAGE

Radius of sphere(mm)	Pressure(Pa)
3	3.58
3.5	3.90
4	4.39
4.5	5.10
5	6.36
5.5	8.71
6	13.09

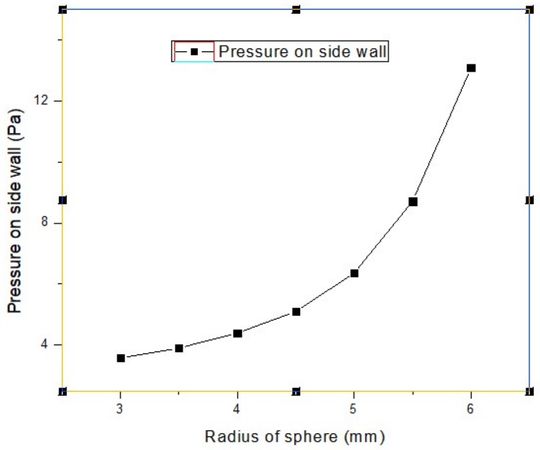

Figure 13. Pressure on artery wall due to spherical blockage

Figure 13 shows the variation of pressure on the arterial wall due to spherical blockage. The graph indicates an exponential rise of the pressure on the side walls. Table 5 shows the pressure experienced by the artery wall due to hemispherical blockage.

TABLE V. PRESSURE ON ARTERY WALL DUE TO HEMISPHERICAL BLOCKAGE

Radius of sphere(mm)	Pressure(Pa)
4	3.74
5	4.04
6	4.82
7	7.29
8	17.59
9	96.91

Figure 14 shows the variation of pressure on the atrial wall due to the hemispherical blockage. Again, we find an exponential increase of pressure on the side wall of the artery. This graph shows an abrupt reading when the radius of hemispheres reaches 9 mm. This is the point where both hemispheres almost touch each other, as shown in Figure 9. The side wall pressure of the healthy artery is found to be 3.13 Pa.

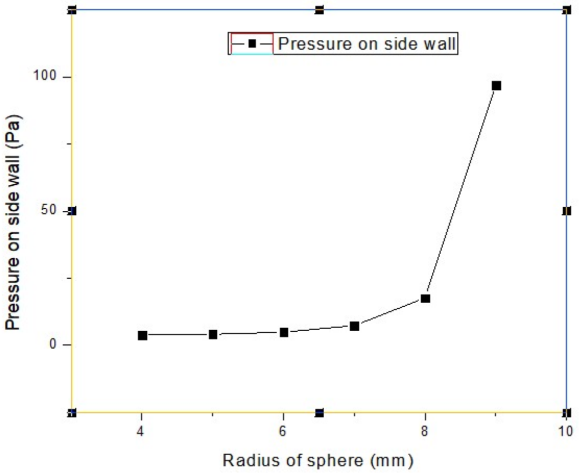

Figure 14. Pressure experienced by artery wall due to hemispherical blockage

IV. CONCLUSION

In this paper, the blood flow in the blood vessels with different shapes and sizes of blockages in the carotid artery has been studies. The velocity and pressure of blood have been studied in each case. While comparing the two types of blockages, we see that one with spherical blockage rises exponentially and the other one shows an abrupt rise when the fat covers most of the cross section of the artery. Clearly, this gives us the intuitive idea that the hemispherical blockage from both walls is very dangerous. Also, another point that can be learned is that when the blockage is small there is not much pressure on the walls, but since it increases exponentially it should be detected at early stage, because as it keeps on accumulating it can be proved fatal and might even lead to burst of the artery.

REFERENCES

[1] J. Blazek, “Computational fluid dynamics: Principles and applications”, Elsevier, ISBN 0 08 04 3009 0, 2001.

[2] B. Radic, “Diagnosis and Treatment of Carotid Artery Stenosis”, J Neurol Stroke 7(3): 00238, 2017. DOI: 10.15406/jnsk.2017.07.00238.

[3] J.T. Salonen, R. Salonen, “Ultrasonographically assessed carotid morphology and the risk of coronary heart disease. Arterioscler”, Thromb 1991; 11:1245-49.

[4] G.B. Mancini, B. Dahlof, J. Diez, “Surrogate markers for cardiovascular disease: structural markers”, Circulation 2004; 109: IV22–IV30.